
The Gravitational Wave Toolbox: modelling electromagnetic counterparts of gravitational wave sources

Kai Sebastian Paul Hendriks



Radboud Universiteit

Master thesis
Department of Astrophysics
Radboud University

First supervisor: Prof. Dr. Gijs Nelemans
Second supervisor: Dr. Shu-Xu Yi

Nijmegen, 15th July, 2021

Abstract

In recent years, the field of gravitational wave (GW) physics has become a central part of astrophysics. As a result of this, an increasing number of physicists, both within and outside the GW community will be using GW observations in their research projects. Therefore, especially now, it is of the utmost importance that information about GW sources and their detectability remains easily accessible. The Gravitational Wave Toolbox (<https://gw-universe.org>) is a tool that aims to take care of this task. It is a user-friendly program, with which one can make quick and efficient computations related to the detectability of GW sources and the properties of GW detectors. As of yet, the Toolbox does not include the possibility to simulate electromagnetic (EM) counterparts (e.g. short gamma-ray burst, kilonovae) of GW events. As we are currently at the start of a multi-messenger astronomy era, joint GW-EM observations have become a very important aspect of GW physics. As such, inclusion of EM signatures of GW sources in the Toolbox would significantly increase the usability and the applicability of this program. The aim of this study is to add models of EM counterparts to GW sources to the GW Toolbox.

We set up models for short gamma-ray bursts (sGRBs) and kilonovae (KNe), as well as EM output of stellar-mass and supermassive black hole binaries. For our sGRB model, we employ an analytical top-hat jet framework, with which we can simulate the sGRB flux and spectrum. We compare this model with observations of GRB170817A, and find that we can recover this well with typical GRB parameters. To predict KN lightcurves, we make use of the existing program `gwemlightcurves`. In this model, we can use the masses and spins of a binary neutron star (BNS) or black hole - neutron star (BH-NS) to compute the mass and velocity of matter ejecta from the binary. From here, through interpolation with photometric datasets from radiative transfer simulations, we can compute the KN lightcurve in different passbands. We compare this model with observations of AT2017gfo, and conclude that its performance is good enough, even though it slightly underestimates the KN brightness. Additionally, we include and show the results of several order-of-magnitude luminosity estimates for the EM output of stellar-mass and supermassive black hole binaries. Subsequently, we illustrate the synergies and trade-offs between GW detectors and EM instruments by using the Toolbox to simulate a universe filled with GW sources, and computing the peak GRB flux for each of them. Lastly, we include a clear visualisation of how these models will be implemented into the framework of the GW Toolbox.

Contents

1	Introduction	1
1.1	The Gravitational Wave Toolbox	2
1.2	This project	4
2	Models of electromagnetic counterparts	7
2.1	EM counterparts of BNS and BH-NS	7
2.1.1	Conditions for EM signatures of BNS and BH-NS	7
2.1.2	Short gamma-ray bursts (sGRBs)	10
2.1.3	Kilonovae (KNe)	15
2.2	Stellar-mass BBH mergers and their EM output	18
2.2.1	Fast radio bursts as EM counterpart	19
2.2.2	A kicked Hill sphere	20
2.2.3	Bondi-Hoyle-Lyttleton accretion luminosity	20
2.2.4	Accretion luminosity	21
2.3	EM signatures of supermassive BBH mergers	21
2.3.1	Eddington-scale accretion	21
2.3.2	Peak accretion luminosity from magnetohydrodynamic simulations	22
3	Results and discussion	23
3.1	Short gamma-ray bursts	23
3.1.1	General characteristics of the model	23
3.1.2	Comparison with GRB170817A	30
3.2	Kilonovae	34
3.2.1	General KN characteristics and outcome of the model	35
3.2.2	Comparison with AT2017gfo	35
3.3	Stellar mass binary black holes	40
3.4	Supermassive black hole binaries	41
3.5	Toolbox and EM counterparts	41
3.5.1	GWs	43
3.5.2	Joint GW-EM detections	44
4	Towards implementation	48
5	Summary & conclusion	52
6	Acknowledgements	54
	Bibliography	60

1 Introduction

Ever since the first direct detection of gravitational waves (GWs) by the Laser Interferometer Gravitational-Wave Observatory (LIGO, [2]) in 2015 [5], the field of GW physics has been a booming business. As of yet, all GW signals that have been detected originate from compact objects that revolve around each other in a binary system. Compact objects are the remnants of stars at the very end of their lifetime. The interior of stars evolves as a result of nuclear fusion; starting from hydrogen, increasingly heavy elements are created. During this process, the gas pressure outwards that results from the fusion energy release needs to balance the gravitational pull of the star itself inwards. Fusion halts (i.e. the life of the star ends) when not enough energy can be released from fusion to take care of this balance, after which the star is compressed by its own gravity and implodes. The nature of the resulting stellar remnant, which is a compact object, depends on its mass: a white dwarf (WD, up to $1.4M_{\odot}$) where electron degeneracy pressure balances gravity, a neutron star (NS, between 1.4 and $\sim 2M_{\odot}$) where the neutron degeneracy pressure balances gravity, or a black hole (BH, for masses above $2M_{\odot}$) where the neutron degeneracy pressure is not strong enough, and the entire system collapses [52, 47]. These compact objects can exist in binaries: e.g. two BHs revolve around one another, while they lose angular momentum and eventually merge to form a single, more massive BH. These angular momentum losses are a result of GWs released by such a binary; much like ripples in a pond, this radiation propagates away from the system, while stretching and compressing the space through which it travels, including (eventually) earth itself where we detect them.

The first detected GW signal originated from a merging binary black hole (BBH) system. Naturally, this was extremely significant as it confirmed the existence of GWs predicted by Albert Einstein, about 100 years prior. Now, arguably even more important than the detection of this BBH was a different observation of GWs, in August 2017; this time, a binary neutron star (BNS) was spotted by both LIGO and Virgo (see [7]) [4]. This observation was a scientific breakthrough in more ways than one, but one of the main reasons why it is so valuable comes from the fact that the GW detection was accompanied by the observation of an electromagnetic (EM) counterpart originating from the same binary [3]. The *Fermi* Gamma-Ray Burst Monitor observed a short gamma-ray burst (sGRB) less than two seconds after the peak of the GW signal [26], and multiple telescopes picked up a bright optical transient lasting several days. The latter has now been classified as a kilonova (KN), also resulting from the BNS merger. With these combined GW (GW170817) and electromagnetic (GRB170817A and AT2017gfo) measurements, we have since entered a novel era of *multi-messenger astronomy*. We are now capable of observing the same objects or events in the universe not only electromagnetically, but also gravitationally. The relevance of this is extremely substantial: the ability to observe from two different channels does not only make the measurements more precise, it also generally provides us with more information regarding the source in question. In essence, we now have multiple sense organs to look at the universe.

Evidently, in the near future, the number of GW and combined GW-EM detections

will only continue to grow, as well as the variety of GW sources that we will be able to study. With planned GW instruments and improvements on our current detectors, we will soon observe GW sources in a wide frequency range. At the high end of the spectrum (beyond 10 Hz), covered by the likes of advanced LIGO [30] and Virgo [7], we will observe objects such as BBHs, BNSs, black hole-neutron star (BH-NS) mergers, and supernova explosions [51]. A highly-anticipated prospect for this part of the frequency range is the Einstein Telescope [43], a planned future ground-based detector that will be able to observe such sources with an even higher sensitivity. The mid-frequency range of $10^{-3} - 1$ Hz is not covered by any current detectors, but projects such as the planned Laser Interferometer Space Antenna (LISA, [8]) will change that. This range corresponds to the late inspiral phase of supermassive black hole binaries (SMBHBs), and extreme mass ratio inspirals (EMRI). Also white dwarf (WD) binaries may be within this range, and their GWs could be picked up by LISA [49]. Frequencies below 10^{-3} Hz and down to 10^{-8} Hz will be within the sensitivity range of so-called pulsar timing arrays (PTAs) [32]. PTAs can map GW signals by monitoring variations in the time-of-arrival of EM signals from pulsars. With this method, a main goal of PTAs is to search for the presence of a stochastic low-frequency GW background signal of which the nature is still unclear. Current PTA projects exist (e.g. IPTA [63]), but are still looking to make their first GW detection and require a higher sensitivity to do so.

1.1 The Gravitational Wave Toolbox

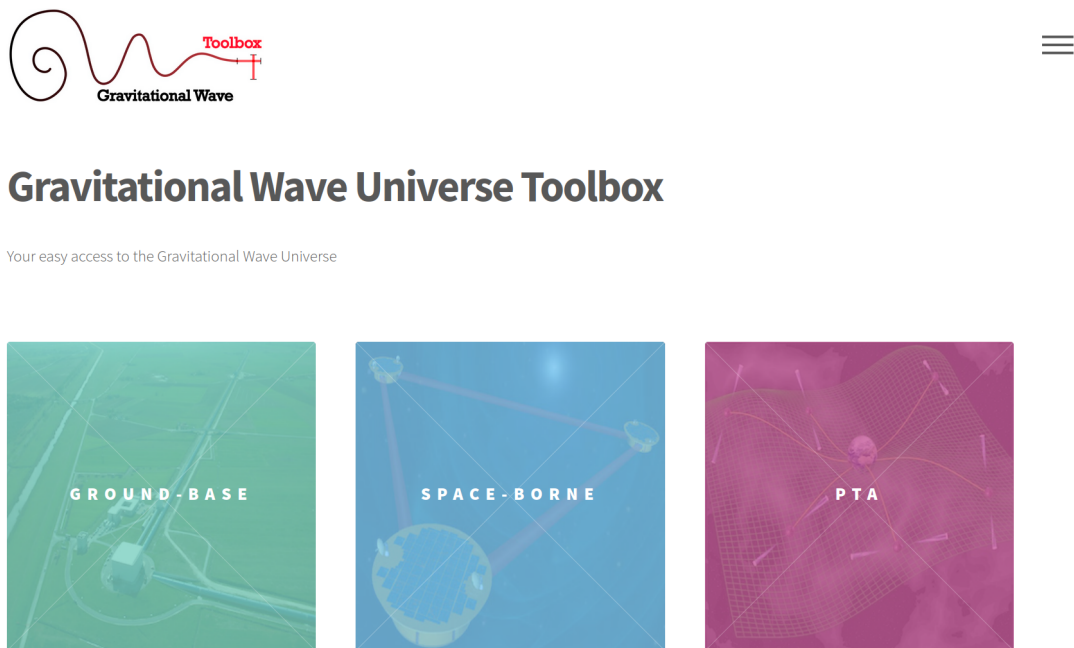


Figure 1: Homepage of the GW Toolbox, at <https://gw-universe.org>.

In the ever-expanding field of GW physics, it is important that the accessibility of information about GW sources and their detectability remains of good quality. Evidently, this is useful for those within the GW community. More so, due to the emerging nature of GW astrophysics as a central part of astronomy, also an increasing number of scientists *outside* the GW community will be using GW observations in their own projects. Therefore, they are especially in need of easily accessible tools to gain insight into GW detections. For example, astronomers interested in populations and stellar evolution might seek information within GW physics. They may need to investigate the characteristics of and distances to compact objects, including those in binaries, within the universe. All of this information could be gathered from simulations of GW events. Additionally, research of those within fundamental high-energy physics can overlap with GW astrophysics. Scientists that study NS interior and exotic matter could be in need of estimates of the number of NS mergers that GW detectors can observe, in order to know on how many NSs their theories can be tested. Moreover, e.g. the stochastic GW background, which is a continuous source of GW emission throughout the universe of which the nature is unknown, has been a major topic within cosmology. Therefore, cosmologists that study this, would be helped tremendously if there would be some easily-accessible tool that can predict GW detections of this source. These are just three examples, and perhaps there exist even more obvious ones. GW physics can overlap in many other ways with different disciplines within physics. Clearly, the versatility of GW astrophysics is both an asset and a curse; where this branch is generally an enrichment of physics itself, it also means that there are many physicists doing research that is linked to GWs, who are not actually GW experts. For them, highly technical and computationally costly sources that should provide them with GW-related information for their research are extremely inconvenient.

Clearly, the need for an automated tool that provides information about GW sources and detectabilities for both experts and non-experts is sky high. The *Gravitational Wave Universe Toolbox* [67], or in short *GW Toolbox*, aims to be exactly this. Designed for a broad audience, the Toolbox is an interactive program that works online (at <https://gw-universe.org>) or as a Python package¹, which serves as a tool to perform quick and efficient computations related to GW detections. In Fig. 1, we depict the current home page of the Toolbox, where Fig. 2 shows the page on which the user can study GW and detector characteristics for ground-based observatories (like LIGO, Virgo, or ET). We see that the user has to select a combination of input parameters: a type of GW detector, a type of GW sources, a time window within which the detector is active, a signal-to-noise ratio (SNR), and a cosmological model. With a specified set of input parameters, the Toolbox engine simulates a universe that is filled with the chosen type of GW source (e.g. BBHs). It runs the specified detector for the given time window, and saves the properties of all detected GW events of the chosen type. As visible in Fig. 2, the output is threefold: the program prints the detector sensitivity curve, number of detected GW events of the specified kind, and a table which we call the "catalogue". This

¹The Python package is available at <https://bitbucket.org/radboudradiolab/gwtoolbox>.

table contains the properties of the detected GW sources: e.g. redshift, distance, masses, and spins. The catalogue can be downloaded, to allow for further investigation by the user. These steps can be performed for a large variety of GW sources and detectors. We can simulate detections of BBH, BNS, or BH-NS with ground-based observatories (LIGO, Virgo, ET, KAGRA, and customised LIGO/Virgo), whereas SMBHBs, WD binaries and EMRIs can be studied with the space-observatory option (LISA). Additionally, the Toolbox includes the possibility to explore the stochastic GW background and individual SMBHBs with both current and future PTAs.

1.2 This project

As of yet, the Toolbox does not include the possibility to simulate electromagnetic counterparts of its GW events. Since we have established the significance of the multi-messenger astronomy era, it is clear that adding models of EM counterparts would not only be logical, but would also largely increase the usability of the Toolbox. An implementation one could think of is e.g. the possibility to simulate BNS GW detections, *including* information on how many of these will result in a GRB, and what fraction of these GRBs will be detected by some high energy satellite. Additionally, e.g. photometric properties of KN lightcurves returned by the Toolbox would be a huge added value. For example, these additions would be useful for astronomers who regularly observe GRBs and may be in need of quick estimates of the frequency with which joint GW-GRB detections will be done with future, more accurate GW observatories. For the same people, the Toolbox can be a pathway towards insights into updates to current GRB detectors. By how much would the Fermi/GBM flux detection threshold need to improve to see a significant increase in joint GW-EM detections? A question like this could easily be answered by an EM counterpart module within the Toolbox. Moreover, e.g. theorists that study the nuclear evolution of the universe may have an interest in KNe lightcurves, as these represent the decay of newly formed elements after BNS or BH-NS mergers. The Toolbox functions as an easily-accessible link between KN lightcurves and the mergers they originate from, to provide said theorists with insight on KN progenitors and the origin of elements. Also for those within the GW community, addition of EM counterparts to the Toolbox would be a huge advantage. For those working for LIGO, Virgo or KAGRA, estimates of frequency of joint GW-EM detections can assist in planning future joint observation campaigns. Additionally, predictions for the EM properties of GW sources in the sensitivity range of future detectors such as the ET and LISA can significantly strengthen the science case for those particular detectors. Again, these are merely a few of many possible examples in which a Toolbox that contains EM counterparts is very useful. In general, addition of EM counterparts to GW sources would allow for investigation of the synergies and trade-offs between GW and EM detections in numerous different ways.

In view of its extremely high potential and the vast amount of new possibilities that it can generate, in this thesis, we aspire to include EM output in the Toolbox. In other

words, the aim of this study is **to add models of electromagnetic counterparts to the GW sources in the GW Toolbox**. To achieve this, we have collected information from numerous studies and adapted this, to eventually create pieces of Python code that are able compute the spectrum, lightcurve or luminosity of each possible EM counterpart, based on the source properties from the GW detections.

In this thesis, we will give a detailed report of the findings and results obtained during this project. In Section 2, we will provide a detailed overview of all EM models that are to be added to the Toolbox and thoroughly explain each and every one of them. Per GW source in the Toolbox, we list all EM signatures that we investigated, and include a framework for each of these. Subsequently, in Section 3, we show the resulting spectra and lightcurves of our models, discuss their validity and accuracy. Additionally, we will demonstrate some of the new possibilities the Toolbox after inclusion of our models. After this, in Section 4, we will highlight how the EM models will be implemented into the framework of the Toolbox. Finally, all main findings will be summarised in Section 5.

Ground-based observatories



INPUT :

Detector:
advanced LIGO (in O3a)

Event types:
Black Hole Binary Mergers

Population model for BHBH
Parameterization I (default param.)

Time [days]: 3650 **SNR-threshold:** 8

Cosmology:
Flat Λ CDM - Planck15

Desired outputs:

- Number of Detection
- Sensitivity Curve
- Catalogue

Maximum number of events to generate:
100

Simulate uncertainties list detectabilites

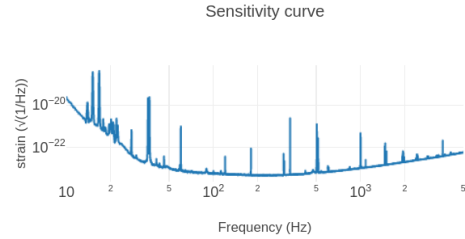
Takes a few minutes. Heavy task may cause timeout error. In this case, we recommend to run the python package locally.

MEANING OF CATALOGUE COLUMNS

- m1: mass of the primary star, in unit of solar masses;
- m2: mass of the secondary star, in unit of solar masses;
- z: cosmological redshift;
- D: luminosity distance in Mpc;
- χ : effective spin;
- d...: uncertainties of corresponding parameters.

RESULT :

SENSITIVITY CURVE :



File Name:

NUMBER OF EVENTS :

Expected number of detection: 396

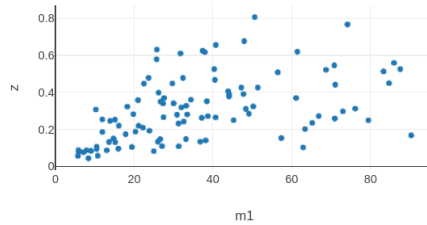
(The actual number of detection is a Poisson variable round the expectation)
P L O T :

X-axis: m1 Y-axis: z

(if x-axis=y-axis, return a histogram)

Logarithmic x-axis Logarithmic y-axis

m1 vs. z



T A B L E :

z	D	m1	m2	χ
0.27	1.43e+3	66.9	64.0	-1.3e-2
0.28	1.48e+3	30.9	19.2	0.028
0.26	1.37e+3	37.2	29.7	0.034
0.61	3.71e+3	31.7	17.5	0.14
0.19	9.7e+2	23.9	12.4	0.058

Figure 2: The main page of the Toolbox, for ground-based GW observatories, on which the user can perform the desired computations.

2 Models of electromagnetic counterparts

In this section, we will carefully explicate all features of models of EM signatures that are to be included in the Toolbox. We will structure this part as follows: per GW source (e.g. BNS or SMBHB), we will list and explain the models for its EM output. The first type of GW event we will discuss, will be BNSs and BH-NSs together, as these have the same EM signatures. We first highlight the conditions that these mergers have to satisfy in order to have EM output, so we know for which of the detected BNS/BH-NS events in the Toolbox we need to compute EM signatures. After that, we will explain the general physics of one of their EM counterparts, namely the sGRBs, when we will subsequently introduce and carefully explicate the sGRB model we wish to employ in the GW Toolbox. This model is able to compute the GRB energy flux as function of time. The second EM model we set up for BNS/BH-NS will be one for KNe, which we will discuss after the sGRB framework. This one can calculate KN lightcurves, in different photometric filters. Afterwards, we will move on to the next type of GW source, namely that of stellar BBHs. Models for these will be less detailed, as we will only provide ways to compute overall EM luminosity from these. Lastly, SMBHBs will be discussed. Also these models will simply contain a luminosity. Limited by the scope of this work, white dwarf (WD) binaries and EMRIs are not included, and will be left for future investigation. To comply with the current coding language of the GW Toolbox, all models are written in Python.

2.1 EM counterparts of BNS and BH-NS

2.1.1 Conditions for EM signatures of BNS and BH-NS

During the final moments in the life of a BNS or BH-NS, the two compact objects merge to form one single massive object. The nature of this merger remnant depends highly on the characteristics of the components of the initial binary; we may be left with either a BH or a NS, where in the latter case we distinguish between a hyper- and supramassive NS [56]. In order to know whether a binary will produce EM output following its GW signal, it is vital to understand the fate of the merger remnant. The remnant is only able to emit EM radiation if it is surrounded by a substantial accretion disk of matter that has been ejected during the merging process [25, 12]. In our model, we need to include the conditions that a BNS or BH-NS needs to satisfy in order to generate EM signatures. To achieve this for the BNS case, we show Fig. 3, which has been taken from [56]. Here, we see a schematic overview of the different scenarios that can occur after a BNS merger. We will discuss these below, after which we will highlight the fate of BH-NS mergers; this is relatively simple compared to BNSs.

All BNS mergers will follow the first two phases (A→B) in Fig. 3. Here, through GW emission, the binary loses angular momentum until the NSs eventually merge. Then, the path splits, where the fate of the merger remnant depends on its mass. We distinguish several remnants: a BH to which the product after phase B promptly collapses

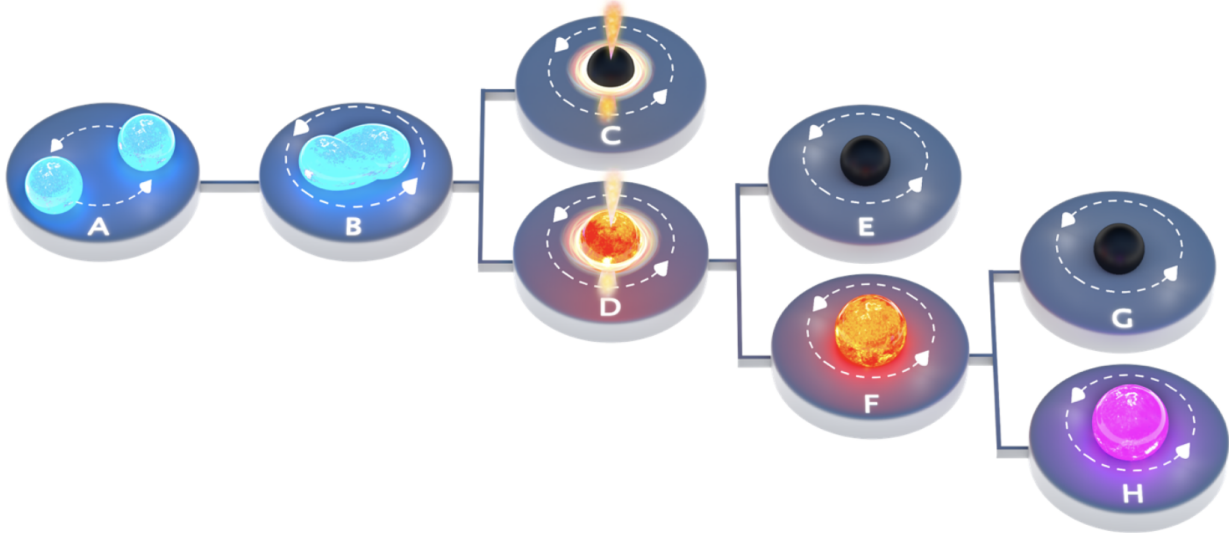


Figure 3: Schematic overview of the different fates of the compact remnant after a BNS merger. The outcome of the merger depends strongly on the remnant mass. Image taken from [56].

(C), a short-lived hypermassive NS that collapses to a BH (D→E), or a supramassive NS that either promptly collapses to a BH (D→F→G) or will remain infinitely stable (D→F→H). For a BH, it is well-known that an accretion disk is generally present, which may launch a jet that triggers a sGRB, and whose ejecta cause a KN. For both short- and long-lived NS, there is still an ongoing debate whether jets and accretion disks can be present. Where there is still quite some uncertainty due to the complexity of these NS remnants, observational evidence strongly suggests that sGRB and KN can occur for NS remnants. This is backed up by numerical simulations [56]. Now, given these different outcomes of BNS mergers, the assumption that every BNS remnant will have an EM counterpart, definitely seems realistic. Therefore, also keeping in mind the aims of the GW Toolbox, we will make the assumption that each BNS event that is simulated in the Toolbox will be accompanied by a sGRB and KN.

As briefly mentioned earlier, the argument for the BH-NS is much simpler. We know for a fact that not all BH-NS mergers will be able to form disks and generate EM signatures. In some BH-NSs, tidal forces tear apart the NS, after which the NS material is partially swallowed by the black hole and partially remains around the BH as a rotating accretion disk. If the tidal radius R_{tid} , i.e. the distance from the black hole where tidal disruption sets in, lies within R_{ISCO} , the radius of the innermost stable circular orbit around the BH, the NS will not be tidally disrupted and will be swallowed by the BH in its entirety. In that case, there will be no accretion disk, and therefore likely no EM output. Given that $R_{\text{tid}} \propto M_{\text{BH}}^{1/3}$, and $R_{\text{ISCO}} \propto M_{\text{BH}}$, this is more likely to happen for a BH-NS with larger BH mass. In our model, we implement this condition: if $R_{\text{tid}} > R_{\text{ISCO}}$, a sizeable accretion disk will form and the remnant will produce a sGRB and KN [25].

2 Models of electromagnetic counterparts

We use $R_{\text{tid}} = (M_{\text{BH}}/M_{\text{NS}})^{1/3} R_{\text{NS}}$, and for R_{ISCO} , we use the Kerr definition [31] of

$$R_{\text{ISCO}} = \frac{GM}{c^2} \left(3 + Z_2 \pm \sqrt{(3 - Z_1)(3 + Z_1 + 2Z_2)} \right), \quad (1)$$

with $Z_1 = 1 + (1 + \chi^2)^{1/3}((1 + \chi)^{1/3} + (1 - \chi)^{1/3})$, and $Z_2 = \sqrt{3\chi^2 + Z_1^2}$. Here, χ is the total spin of the remnant BH.

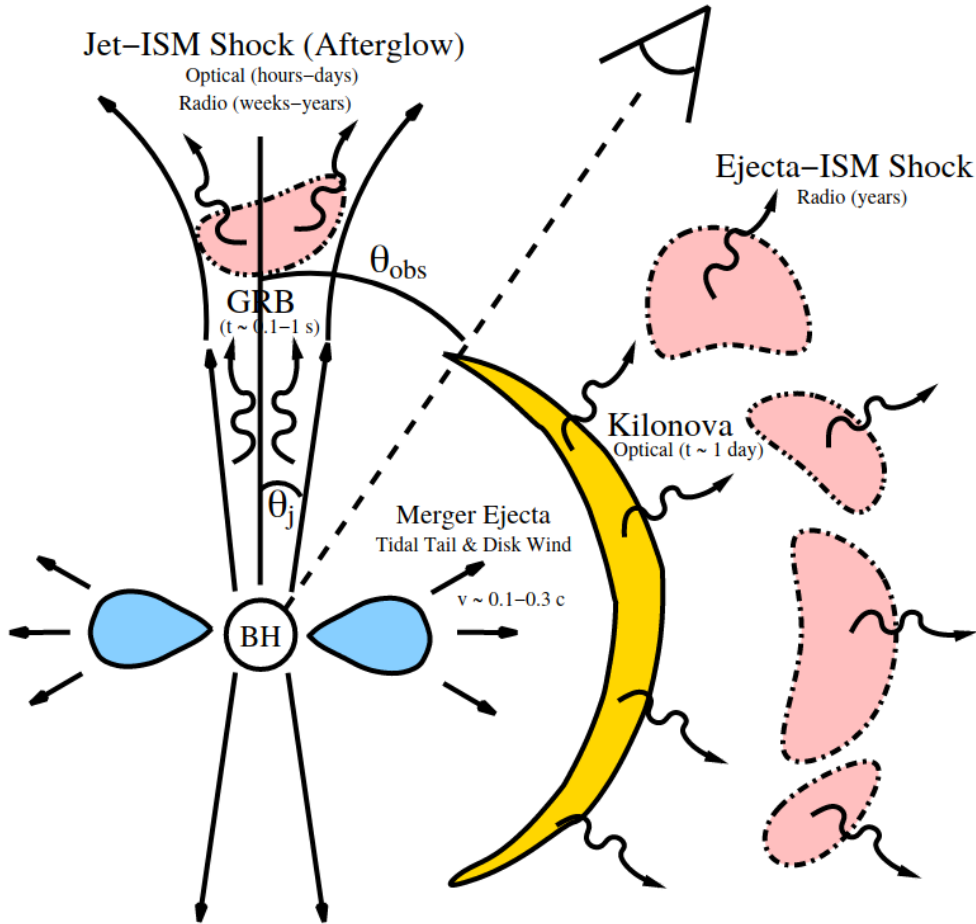


Figure 4: Schematic overview of the electromagnetic follow-up as a result of a merged BNS or BH-NS. Figure has been taken from [45].

Finally, having discussed all conditions for EM signatures, we depict in Fig. 4 a simplified overview of all EM counterparts that can occur after either a BNS or a BH-NS has merged. Subsequent to formation of the merger remnant (either a BH or a massive NS), surrounded by a disk of matter that has been ejected during the merger phase, a relativistic jet may be launched. Shock mechanisms within this jet trigger a highly energetic *short gamma-ray burst* (sGRB) lasting several seconds; the exact details of this will be explained in Section 2.1.2. Moreover, the presence of the mass ejecta that make up the disk and its surroundings may eventually give rise to a *kilonova* (KN). In this

process, the radioactive decay of heavy r-process nuclei that have been formed during the merger causes a bright optical/IR transient, lasting several days [33, 52]. This will be investigated in more detail in Section 2.1.3. Additionally, interactions between the jet and the interstellar medium (ISM) as well as the ejecta and the ISM can cause a longer, less energetic afterglow.

As we know, thus far, the sole EM observations from a BNS or BH-NS are the prompt emission and afterglow of sGRB (GRB170817A), and KN (AT2017gfo) [3]. Given the fact that these two types of EM correspond to BNSs, which make up the largest population of GW sources that can potentially be observed in multi-messenger fashions, we simulate these in more detail. In Section 2.1.2 and 2.1.3, we will discuss the sGRB and KN model that we employ. This will be done through clear step-by-step explanations of each aspect of the models.

2.1.2 Short gamma-ray bursts (sGRBs)

As mentioned before, shock mechanisms related to the propagation of the relativistic jet can cause highly energetic bursts. The shock mechanism that is generally accepted to be associated with the sGRB is the so-called *internal shock model* [54, 34, 41, 64]. In Fig. 5, we show the formation of the sGRB due to the internal shock in a schematic fashion. This process starts at the final moments of the BNS or BH-NS (Fig. 5a). The merger remnant (depicted as a BH here) of such a system can form a large accretion disk, which contains matter from the original NSs [17]. This setup triggers the launch of a relativistic jet (e.g. through the Blandford-Znajek mechanism [13]), consisting of ionised NS matter (Fig. 5b). The launch of this jet may not be instantaneous, but rather divided over multiple relativistic shells that are launched after one another. This is depicted in Fig. 5c. In this scenario, it is possible that a shell launched at time t_1 (shell 1 in Fig. 5c) has a lower velocity than one launched at a *later* time t_2 (shell 2). Inevitably, the two shells eventually collide at a distance r_0 from the central engine. The shock that results subsequently triggers the launch of a sGRB (Fig. 5d), which lasts for several seconds at extremely high energies up to 10^{51} ergs [53].

The mathematical framework of sGRB model that we describe below is entirely based on a 2001 study Ioka & Nakamura [34], which in turn combines the efforts of [65] and [53]. Our reasoning for choosing this analytical model is manifold. First of all, it is relatively simplistic, but not oversimplified. This is perfectly in line with the aims of the GW Toolbox. We seek a model of which the level of complexity is low enough that it does not require a lengthy computation time, while still having an acceptable accuracy. A second reason for choosing this model is the fact that it allows for improvement; if we wish to slightly increase the complexity of the model, we can, due to the way it is set up, quite easily perform this action. We will come back to this once we have explained the model framework.

The setup of our model is depicted in Fig. 6. We use spherical coordinate system $\mathbf{r} = (r, \theta, \phi)$, in the lab frame. The $\theta = 0$ axis points towards the observer. We, the observer, find ourselves at a distance D from the central engine that is the origin of the

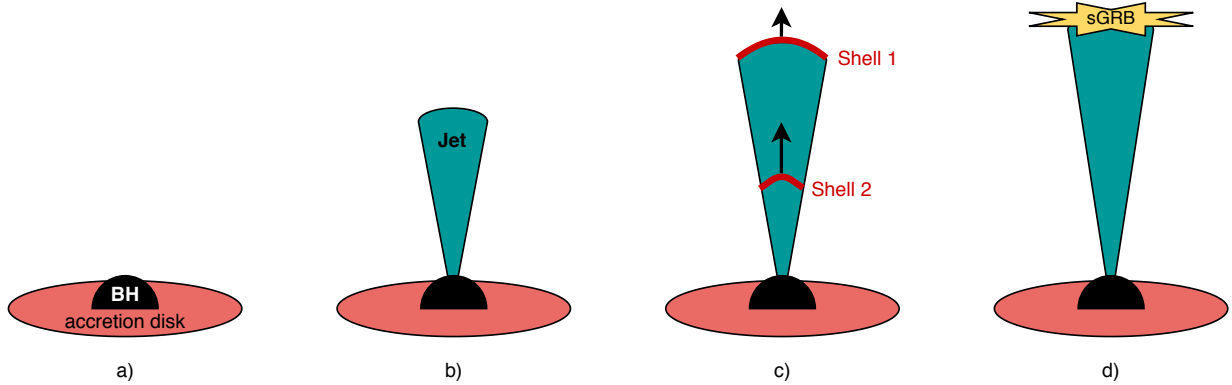


Figure 5: Schematic overview of the main phases to the internal shock model, eventually triggering the sGRB.

jet formation. The jet, as shown in Fig. 6, has an opening angle $\Delta\theta$ and some emission region, from which we will receive the GRB radiation. Additionally, we define an angle α ; imagine we have light ray that is created somewhere in the jet, and points towards the observer. The angle $\alpha = r \sin \theta / D$ is the angle that this ray makes with the $\theta = 0$ axis. Note that D is generally very large, so α will be vanishingly small. Lastly, we introduce the viewing angle θ_v . This allows us to describe scenarios where the jet is tilted with respect to the observer. Setups with a non-zero viewing angle are depicted in the middle and bottom panels of Fig. 6.

In order to be able to predict the lightcurve and spectrum from a sGRB that is to be included in the Toolbox, we need to know how the photon flux evolves over time. The generic formula to compute the flux of an emitting thin shell that moves radially outwards with Lorentz factor $\gamma = 1/(1 - \beta^2)^{1/2}$, as a function of time in the observer frame (T) and photon frequency ν , is:

$$F_\nu(T) = \frac{\nu D}{\gamma \beta} \int_0^{2\pi} d\phi \int_0^{\alpha_m} \alpha^2 d\alpha \int_{\nu\gamma(1-\beta)}^{\nu\gamma(1+\beta)} \frac{d\nu' j'_{\nu'}(\Omega'_d, \mathbf{r}, t)}{\nu'^2 (1 - \mu^2)^{3/2}}, \quad (2)$$

in in $\text{ergs s}^{-1} \text{cm}^{-2} \text{Hz}^{-1}$. Here, $\mu = (1 - \nu'/\gamma\nu)/\beta = \cos\theta$, where ν' is the frequency in the co-moving frame. The angle α_m is the largest value that α can have: from light rays originating from the very edge of the cone. The relationship between the observer time T and source time t can be seen from the geometry in Fig. 6: imagine a photon emitted from the origin at $t = 0$, and some later time t_0 a photon is emitted from a certain radius r_0 and angle θ_0 . The *difference in arrival time* between the photon emitted at t_0 from (r_0, θ_0) , and the photon emitted at $t = 0$ is $t_0 - r_0 \cos \theta_0 / c$. This difference in arrival time is exactly how we define T . We generalise and find the $T - t$ relationship:

$$T = t - \frac{r\mu}{c}. \quad (3)$$

There is one quantity in Eq. 2 that we have not discussed yet, which requires more attention because of its significance. This quantity is $j'_{\nu'}$, the emissivity in the comoving

2 Models of electromagnetic counterparts

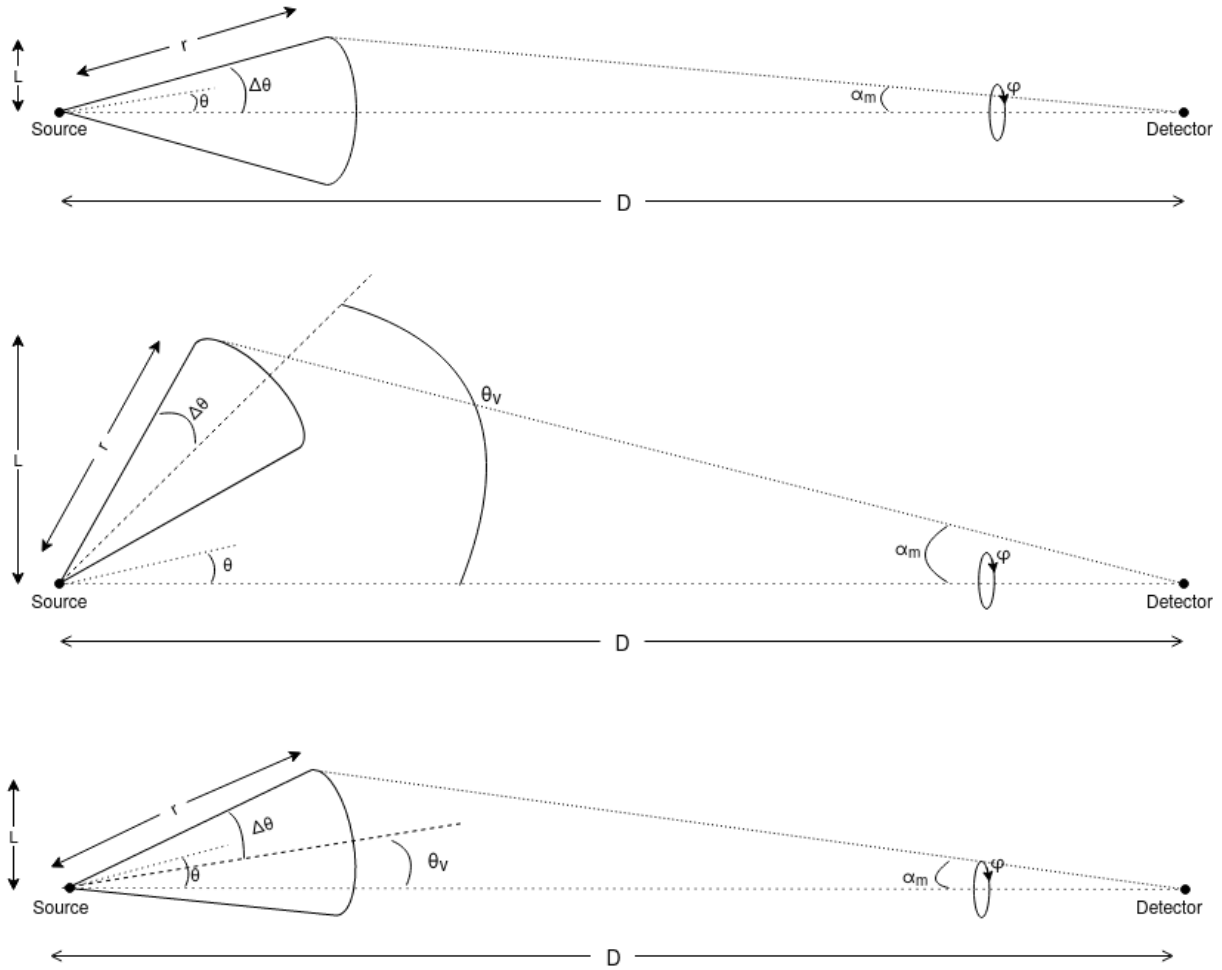


Figure 6: General setup of our jet structure model that produces the sGRB. Bottom panel: face-on view, i.e. a θ_v of 0. Middle panel: $\theta_v > \Delta\theta$, so we are outside of the GRB beam. Bottom panel: $\theta_v < \Delta\theta$, i.e. we find ourselves within the beam. Drawings are inspired by [65].

2 Models of electromagnetic counterparts

frame, measured in units of $\text{ergs s}^{-1} \text{cm}^{-3} \text{Hz}^{-1} \text{sr}^{-1}$. In here, we specify the jet structure and emission mechanisms. $j'_{\nu'}$ is defined as

$$j'_{\nu'} = A_0 f(\nu') \pi(t) \psi(r) \Pi(\Omega). \quad (4)$$

Here, $\pi(t)$ and $\pi(r)$ are the temporal and radial distribution of the emission, respectively. $\Pi(\Omega)$ is the angular distribution of the emitted radiation, so it essentially describes the angular structure of the relativistic jet. $f(\nu')$ represents the spectral shape, and A_0 is a scaling constant that depends on the total amount of energy liberated in the GRB. Now, as we mentioned earlier, the way this particular model is set up is extremely convenient for the Toolbox, which requires a balance between computational efficiency and accuracy. With Eq. 4, we are completely free in making our model as simplified or complex as possible by choosing any distribution we want for the four different functions within Eq. 4. Additionally, if, for example, the $\pi(r)$ distribution we use turns out to be an oversimplification and we would prefer a slightly more sophisticated one, it is very easy to implement this; all one has to do is plug the new $\pi(r)$ into Eq. 4. One should note that the final integral of Eq. 2 would get more complicated in this scenario, so simplification of the integral would require some extra effort.

In the Toolbox, we make the following choices for the quantities within Eq. 4. We follow [34]:

$$\pi(t) = \delta(t - t_0), \quad (5)$$

$$\psi(r) = \delta(r - r_0), \quad (6)$$

$$\Pi(\Omega) = H(\Delta\theta - |\theta - \theta_v|) H \left[\cos\phi - \left(\frac{\cos\Delta\theta - \cos\theta_v \cos\theta}{\sin\theta_v \sin\theta} \right) \right]. \quad (7)$$

This represents instantaneous emission at time t_0 , from radius r_0 . Our $\Pi(\Omega)$ describes a so-called *top-hat jet*, where $H(\dots)$ represents the Heaviside step function. Geometrically, we can view this setup as a cone-shaped jet with a spherical cap. We have, essentially, already depicted this in Fig. 6. All emission in this system comes only from the infinitesimally small spherical cap. For the emission spectrum, we approximate the Band spectrum ([10]) that has proven to successfully model sGRB spectra:

$$f(\nu') = \left(\frac{\nu'}{\nu'_0} \right)^{1+\alpha_B} \left[1 + \left(\frac{\nu'}{\nu'_0} \right)^s \right]^{(\beta_B - \alpha_B)/s}. \quad (8)$$

In order to fit with observations, one can tune α_B , β_B , and s accordingly. Throughout this study, we follow [33] and set $\alpha_B = -1$, $\beta_B = -2.2$ and $s = 1$. The break frequency of this broken power law spectrum is regulated by ν'_0 . For now, we leave this as a free parameter of the model.

Additionally, we need to make sensible choices for r_0 and t_0 . For r_0 , we follow [33] by assuming a typical value of $r_0 = 10^{13}$ cm. It should be noted that r_0 can generally be approximated by $\sim \beta c \gamma^2 \delta T$, where δT is the time between the launch of two relativistic shells. However, values for δT are highly uncertain, so it is more sensible to simply

2 Models of electromagnetic counterparts

adopt some typical value for r_0 . For t_0 , we can use a relatively simple expression. From the perspective of the central engine (so the observer that measures in t rather than T), the shock and GRB launch happens at time t_0 , when the jet has travelled to r_0 . Since the jet moves at a speed of βc , we get:

$$t_0 = \frac{r_0}{\beta c}. \quad (9)$$

The scaling constant A_0 , the final ingredient, is related to the total energy output of the sGRB by

$$\frac{1}{2} E_{GRB} = \int \int \int j'_{\nu'} d\Omega r^2 dr d\nu' dt \quad (10)$$

$$= A_0 \int_{-\infty}^{\infty} \delta(t - t_0) dt \int_0^{\infty} f(\nu') d\nu' \int_0^{\infty} r^2 d(r - r_0) dr \quad (11)$$

$$\int_{\theta=0}^{\pi} \int_{\phi=0}^{2\pi} H(\Delta\theta - |\theta - \theta_v|) H \left[\cos \phi - \frac{\cos \Delta\theta - \cos \theta_v \cos \theta}{\sin \theta_v \sin \theta} \right] \sin \theta d\theta d\phi$$

$$= A_0 \int_{-\infty}^{\infty} \delta(t - t_0) dt \int_0^{\infty} f(\nu') d\nu' \int_0^{\infty} r^2 d(r - r_0) dr \quad (12)$$

$$\int_{\theta=0}^{\pi} \int_{\phi=0}^{2\pi} H(\Delta\theta - \theta) \sin \theta d\theta d\phi.$$

In the last step, we simplified the integral by noticing that the total GRB energy does not depend on the viewing angle θ_v . Because of that, we are (only for this computation) allowed to change $\Pi(\Omega)$ to a less complex distribution that assumes a θ_v of zero, as shown in the top panel of Fig. 6. Additionally, one should pay attention to the factor $1/2$ in front of E_{GRB} . We are computing the emission from a single jet, where GRB engines generally have two. Therefore, the energy we calculate on the right-hand side is only *half* of the total GRB energy.

We obtain for A_0 :

$$A_0 = \frac{E_{GRB}}{8\pi r_0^2 \nu'_0 I}, \quad (13)$$

where $I = \int_0^{\pi} H(\Delta\theta - \theta) \sin \theta d\theta$, which we solve numerically. Finding an accurate number for E_{GRB} is extremely complex. For one, this number depends on the mass of the accretion disk around the remnant, which in turn depends on the composition and characteristics of the neutron star(s). As of yet, there is no known exact relation between the NS and disk mass. However, there has been progress in approximations to this relation, through fitting expressions from numerical relativity simulations (see e.g. [48, 12]). Still, there are more uncertainties, such as the conversion efficiency of the disk mass into GRB energy. Therefore, we leave E_{GRB} as a free parameter.

At this point, we have all the ingredients to compute the temporal evolution of F_{ν} according to Eq. 2. Fortunately, with our simplified assumption in Eqs. 5-7, the integral

in Eq. 2 has already been worked out by [34] as:

$$F_\nu(T) = \frac{2cA_0r_0}{D^2} \frac{\Delta\phi(T)f\{\nu\gamma[1 - \beta \cos \theta(T)]\}}{\{\gamma^2[1 - \beta \cos \theta(T)]^2\}}. \quad (14)$$

Here, $\theta(T) = \cos^{-1}\left(1 - \frac{Tc}{r_0}\right)$. For $\Delta\theta > \theta_v$ and $0 < \theta(T) \leq \Delta\theta - \theta$, $\Delta\phi(T) = \pi$. In any other case, $\Delta\phi(T) = \cos^{-1}\left\{\frac{\cos \Delta\theta - \cos \theta(T) \cos \theta_v}{[\sin \theta_v \sin \theta(T)]}\right\}$. Apart from ν and T , the model depends on six event-specific parameters: $\Delta\theta$, θ_v , γ , ν'_0 , E_{GRB} , and D . In Section 3, we will make some choices regarding these, in order to generate sGRB spectra.

2.1.3 Kilonovae (KNe)

As we have established before, KNe are, alongside with sGRBs, a main EM counterpart of BNS and BH-NS mergers. In Fig. 4, we have already been given a schematic of the origin of KNe, and in this section we will build upon this by explaining it more in detail and introducing the model we use in the GW Toolbox.

We include Fig. 7 to once again depict the surroundings of a merged BNS or BH-NS, where this schematic, compared to Fig. 4, highlights the presence of the KN more. From this image, we clearly see that the KN emission comes from two different components. The ejecta depicted in red are the so-called tidal ejecta. For this type, matter is expelled on dynamical timescales of milliseconds. In BNSs, there are two processes that generate these ejecta. First, hydrodynamic forces squeeze out and repel matter at the contact interface between the two stars. Secondly, during interaction between the stars, tidal forces create spiral arms of matter ejecta around the merging NSs. In the BH-NS, mainly tidal forces on the NS take care of the ejection of matter. In both types of merger, the debris around the central object can have enough angular momentum to form an accretion disk. The second type of ejecta, depicted in blue in Fig. 7, is called *wind ejecta*. Neutrino heating and/or magneto-hydrodynamic turbulence generates strong wind outflows out of the disk. The total amounts of tidal and wind ejecta may be of comparable mass. These amounts are highly dependent on the mass and the nature of the initial compact binary [46, 9].

Both ejecta components are highly neutron-rich, which makes them ideal environments for r-process nucleosynthesis. In this process, heavy elements are synthesised by successively capturing neutrons in such a rapid fashion, that the nuclei do not have time to undergo β -decay (see e.g. [52]). This eventually leads to the production of very heavy elements. Still, these elements are radioactive, which means they will eventually decay back to stability. The β -decay and nuclear fission of these elements releases energy, which can power a transient that lasts several days, or even tens of days. Such a transient, i.e. a kilonova, has a lightcurve that is a combination of the energy released by the two individual types of ejecta; these generate photons in different wavebands of the EM spectrum. The tidal ejecta region is very neutron-rich, and will therefore generate heavy elements up to and including the lanthanides (atomic number 57-71).

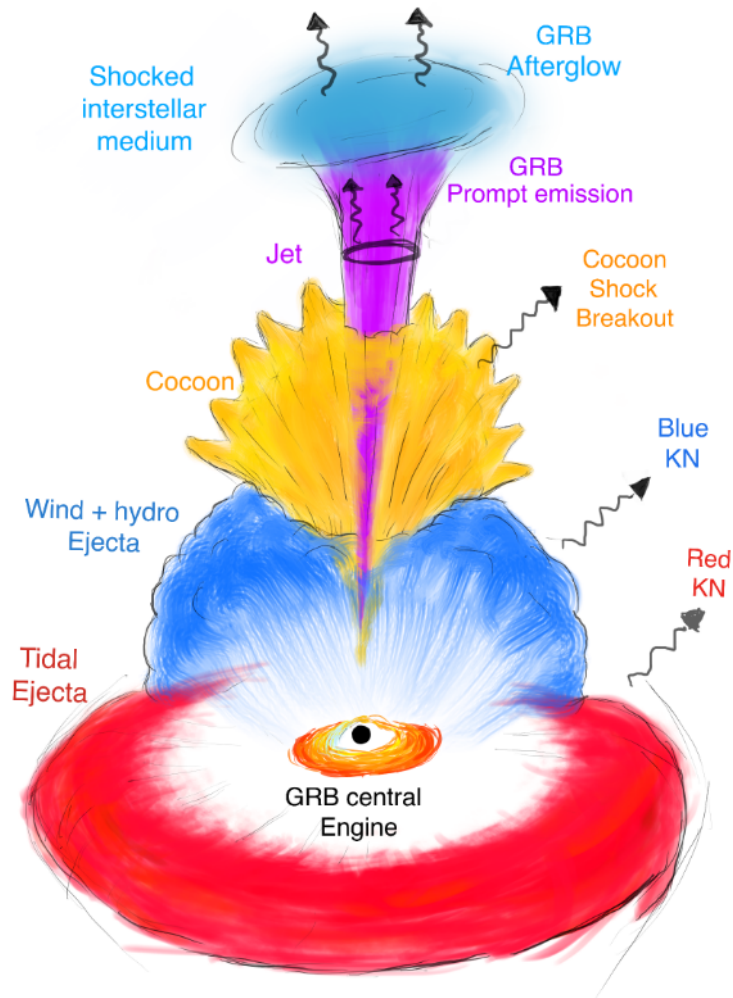


Figure 7: Artist impression of the EM signatures to a BNS or BH-NS merger. This image depicts the same as Fig. 4, however it puts more emphasis on the presence of the KN. Figure taken from [9].

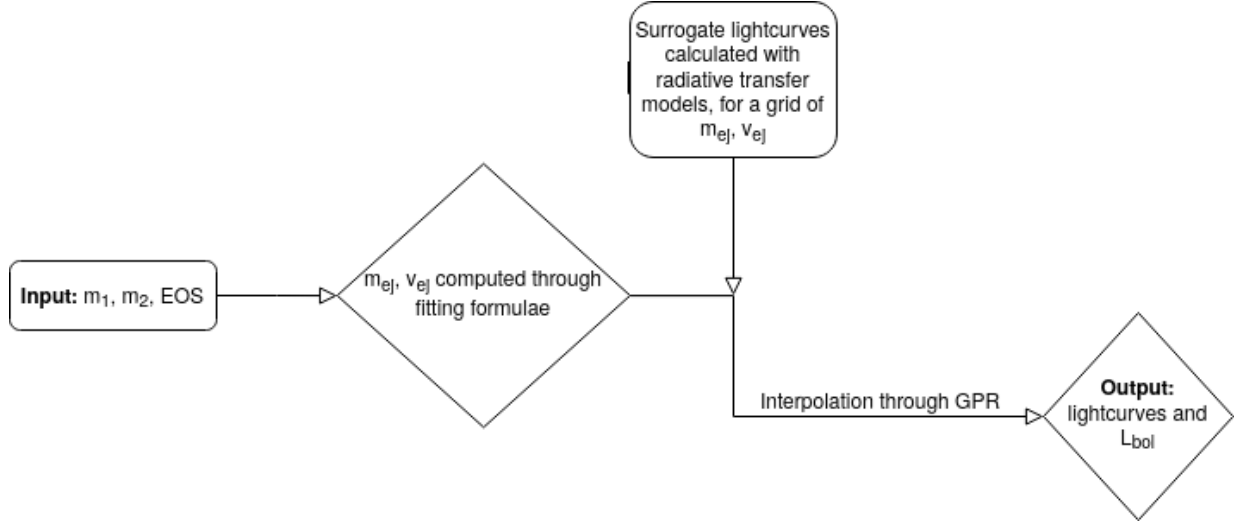


Figure 8: Flowchart that gives an overview of the working of our KN model [61].

The emission from this region is generally seen in the near-infrared (NIR), in the J and K bands. From the onset, the wind ejecta are more proton-rich and will therefore be lanthanide-poor or lanthanide-free. Due to this difference in composition, these ejecta will release energy in different bands than the lanthanide-rich component. The peak emission for this component is in the visual band (R and I), and may even be brighter than the lanthanide-rich component. The ‘red’ and ‘blue’ KNe collectively form the total lightcurve, which is approximately isotropic [9, 46, 22].

In our KN model, we follow [61]. This study employs a method that allows for input of the two component masses, and generates the lightcurve of the resulting KN in a specified passband. The computation of the lightcurve happens in several distinct steps, each of which we will highlight now.

For a clear visualisation of the steps employed by this model, we show in Fig. 8 a flowchart of the procedure. As we see, the input of this model consists of the BNS or BH-NS component masses, accompanied by an equation of state (EOS)² for the NSs. From the input, the model then computes the total ejecta mass m_{ej} and ejecta velocity v_{ej} . This is done through the use of fitting formulae that calculate the disk mass M_{disk} , dynamical ejecta mass m_{ej}^{dyn} , and v_{ej} , all of which are summarised in [61]. The total ejecta mass is then calculated as $m_{ej} = m_{ej}^{dyn} + \zeta M_{disk}$, with $\zeta = 0.15$, based on numerical-relativity simulations. ζ represents the fraction of the disk mass that becomes gravitationally unbound. In other words, ζM_{disk} is the total mass of the tidal ejecta (contributing to the red KN), where m_{ej}^{dyn} corresponds to the mass of the dynamical ejecta (blue KN). Subsequently, with m_{ej} and v_{ej} , the KN lightcurve can be computed. This happens with the help of a so-called *surrogate model*. The surrogate model consists of many sets of

²The equation of state is a vital quantity in modelling the NS interior, as it is an equation that describes the relation between the pressure and density inside the NS.

photometric data (i.e. lightcurves) from simulations that solve the radiative transfer equation in a relativistically expanding medium, based on initial m_{ej} and v_{ej} . Each set of data is the result of a simulation with a certain m_{ej} and v_{ej} , such that the complete dataset from all simulations covers some mass grid, e.g. between 0.001 and 0.1 M_{\odot} , and velocity grid, e.g. between $0.1c$ and $0.4c$. With these grids and their photometric results, we can interpolate to obtain the lightcurve from *any* input m_{ej} , with use of the concept of Gaussian Process Regression (GPR) (see [19]). The output of the model is a set of lightcurves in the g, r, i, z, y, H, J and K photometric bands, as well as the total bolometric luminosity L_{bol} of the system. All these steps can be performed with the Python package `gwemlightcurves`³.

In [61], two different surrogate models are employed: *Model I* [36] and *Model II* [15, 20]. These models differ in the sense that they use different input parameters, apart from m_{ej} and v_{ej} . *Model I* is based on simulations solving the radiative transfer equation that also take as input the lanthanide mass fraction X_{lan} . Rather than computing the lightcurve for lanthanide-rich and lanthanide-poor ejecta separately, it calculates the lightcurve for the total ejecta mass at once, assuming some fraction X_{lan} consists of lanthanides. *Model II*, on the other hand, is different from the geometry-independent and 1-dimensional *Model I*; it does not take X_{lan} as input parameter, but the half-opening angle around the plane of merger of the lanthanide-rich component (Φ), and the inclination angle (θ_{inc}). Where one could think that *Model II* more realistic as it includes a more complex geometry, [61] found that it fails to accurately recover the AT2017gfo lightcurve up to several days after merger. Additionally, the computation time for *Model I* is $O(10s)$ per passband, whereas *Model II* needs $O(5min)$. Therefore, in this study, we only employ *Model I*. We set $X_{\text{lan}} = 10^{-4}$, which is in line with [61] and consistent with the results of [19].

2.2 Stellar-mass BBH mergers and their EM output

The title of this section may seem counter-intuitive, as BBHs that merge in vacuum are generally believed to have no EM counterparts. However, in the accretion disk surrounding a SMBH of an active galactic nucleus (AGN) (see Fig. 9), a BBH merger may well be accompanied by an EM signature [29]. In fact, [28] reports a candidate EM counterpart to the GW190521 observation of a BBH [6]. The EM transient observed by the Zwicky Transient Facility was consistent with the expectations for a kicked BBH merger. Even though this detection in the end did not receive the confirmation as an EM counterpart to a BBH, it may just be a matter of time before this happens for future detections. The BBH merger rate in AGN disks has recently been estimated as $\mathcal{R} \approx (0.002 - 18) \text{ Gpc}^{-3} \text{ yr}^{-1}$ [29]. This is certainly non-negligible, as the most recent estimate for the general BBH merger rate is, with 90% credibility, $\mathcal{R} = 53.2_{-28.8}^{+58.5} \text{ Gpc}^{-3} \text{ yr}^{-1}$ [1]. As of yet, there exists, however, no single clear-cut theory for the mechanism that accounts

³This code is available at <https://github.com/mcoughlin/gwemlightcurves>. For its documentation, see <https://gwemlightcurves.github.io/index.html>.

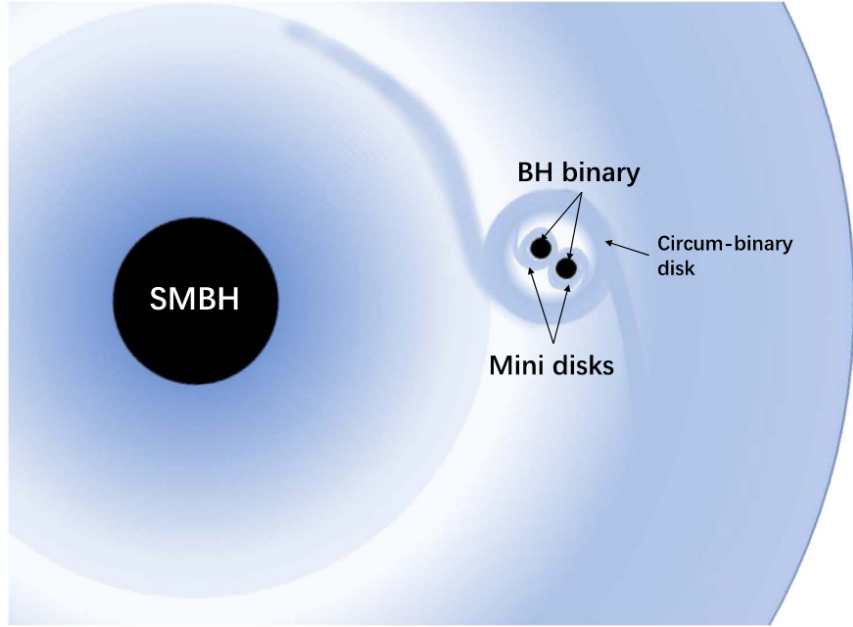


Figure 9: A BBH merger inside the disk of an AGN. Due to the gaseous environment, the binary is surrounded by a circumbinary accretion disk. This disk is porous, which allows for matter to seep through within the cavity that was created by the binary. This may create a pair of mini-disks around the two individual BHs. Figure taken from [66].

for the BBH EM counterpart. In the Toolbox, we will therefore include several models for these counterparts and allow the user to choose one of them while simulating the GW universe with BBH mergers. Additionally, due to the speculative nature of these EM signatures as well as models describing them, providing detailed lightcurves would not only be difficult, but also unnecessary. Therefore, this part of the Toolbox will only return the total luminosity and/or the total flux as an extra column in the simulated catalogue (see Section 4). In the following, we will discuss the four models that we will include in the Toolbox.

2.2.1 Fast radio bursts as EM counterpart

Fig. 9 depicts the scenario in which this model plays a role. We see a BBH within an AGN disk, where the binary is surrounded by a circumbinary disk (CD) as well as two smaller accretion disks around each BH. After the BH coalescence, remnant materials and matter from the CD accretes onto the remnant in a very quick fashion [66]. The EM signature arises from a clumpy jet, that may be launched as a result of high-mass transfer. The fast radio burst (FRB) that takes place has luminosity

$$L_{\text{FRB}} = \frac{8\eta M_{\text{rem}} f_{\text{Edd}}}{2\pi(1 - \cos\theta)} \times 10^{38} \text{ ergs s}^{-1}. \quad (15)$$

2 Models of electromagnetic counterparts

Here, η is the accretion efficiency, M_{rem} is the BH remnant mass, $f_{Edd} = L/L_{Edd}$ is the Eddington ratio of the accretion onto the two BHs, and θ is the jet opening angle. We follow [66] and assume typical values $\eta = 0.1$, $f_{Edd} = 10^1$, and $\theta = 0.1$.

2.2.2 A kicked Hill sphere

When two BHs merge, asymmetries in the system can induce a BH kick; conservation of angular momentum makes sure that the final BH remnant is repelled away in the opposite direction of the final GW signal [27, 16]. [44] reports that BH kicks in AGN disks can trigger optical/UV EM transients. Gravitationally bound gas around the BH (i.e. within the *Hill sphere*, or *sphere of influence*) flies along with the BH, and collides with the surrounding disk gas, which generates an EM transient.

The luminosity of this ram-pressure stripping can be approximated by

$$L_{\text{strip}} \approx 6.34 \times 10^{39} \left(\frac{M_{\text{Hill}}}{M_{\odot}} \right) \left(\frac{v_{\text{kick}}}{10^2 \text{km/s}} \right) \text{ ergs s}^{-1}, \quad (16)$$

where

$$\begin{aligned} M_{\text{Hill}} &= V_{\text{gas}} \rho \\ &= ((4/3)\pi R_H^3 - (2/3)\pi(R_H - H)^2[3R_H - (R_H - H)])\rho, \end{aligned} \quad (17)$$

where $R_H = r(M_{\text{BBH}}/(3M_{\text{SMBH}}))^{1/3}$. Here, r is the distance from the binary to the SMBH, which we set to a fiducial value of $10^3 r_g$. We compute $r_g = GM_{\text{SMBH}}/c^2$. Additionally, we follow [44] and assume the disk height $H \approx r_g$, $v_{\text{kick}} = 10^2 \text{km/s}$ and $\rho = 10^{-10} \text{g/cm}^3$. Hence, the input one needs for this model is the total binary mass, and some assumption for the mass of the SMBH. A fiducial value we use for the latter is $M_{\text{SMBH}} = 10^9 M_{\odot}$.

2.2.3 Bondi-Hoyle-Lyttleton accretion luminosity

A different model that could account for the peak EM emission from BBH mergers is the Bondi-Hoyle-Lyttleton (BHL) luminosity [28]. This scenario may happen in combination with the ram-pressure stripping, and may or may not produce higher luminosities. In this case, after the ram-pressure stripping, nearby gas in the AGN disk is accreted onto the BH remnant. This gives a luminosity of

$$L_{\text{BHL}} \approx 2.5 \times 10^{45} \left(\frac{\eta}{0.1} \right) \left(\frac{M_{\text{BBH}}}{100 M_{\odot}} \right)^2 \left(\frac{v_{\text{kick}}}{200 \text{km/s}} \right)^{-3} \left(\frac{\rho}{10^{-10} \text{g cm}^{-3}} \right) \text{ ergs s}^{-1}. \quad (18)$$

Here, for simplicity, we use the fiducial values $\eta = 0.1$ (accretion efficiency), $v_{\text{kick}} = 200 \text{km s}^{-1}$, and $\rho = 10^{-10} \text{g cm}^{-3}$.

2.2.4 Accretion luminosity

A final possibility for the EM signal was reported by [11]. This model is similar to the BHL luminosity, however this time, we assume the EM output originates from super-Eddington accretion of gas in the AGN disk, *before* merger. We can describe this with luminosity

$$L_{\text{acc}} = 9.52 \times 10^{38} 4\pi\eta \left(\frac{M_{\text{tot}}}{100M_{\odot}} \right) \text{ ergs s}^{-1}. \quad (19)$$

Here, $\eta = L/L_{\text{Edd}}$. A requirement for detectability is that η is at least 10^4 , so for this model we will adopt this number.

2.3 EM signatures of supermassive BBH mergers

For SMBHB with EM signatures, which occur when the SMBHB evolves in a gaseous environment, a widely accepted model does not exist yet. There have been detailed simulations from binary AGN accretion disks before merger ([39, 21, 14, 38, 37]), in the afterglow phase after merger ([58]), and from a post-merger jet ([68]). However, predictions are very model-dependent, and the observations so far cannot break the uncertainties. Therefore we include two models that we find representative and general as example. More models can be added in the future. For now, it is important that we include at least some order-of-magnitude estimation of the peak luminosity at merger. LISA-like detectors will be able to detect GWs days or even weeks before merger [42], so there will generally be plenty of time after a GW detection to start an EM observing campaign. In case the Toolbox can provide a luminosity estimate, this will assist in painting a more quantitative picture of such a joint observation. Similar to the stellar BBH case, the luminosity will simply be an extra column in the output catalogue of the Toolbox.

2.3.1 Eddington-scale accretion

The first model we will implement is taken from [40]. This study shows that in the scenario that the heat deposited in the gas near a SMBHB is proportional to the total SMBHB mass and the gas is optically thick, the luminosity at merger will be of the order of the Eddington luminosity, independent of the total gas mass. It should be noted that the likeliness of this scenario has its uncertainties, but it is still among the possibilities. The luminosity of this prompt EM radiation that results from accretion can be described as:

$$L_{\text{acc}} \approx 10^{45} \epsilon^{1/2} M_7 \text{ ergs s}^{-1}, \quad (20)$$

where ϵ is the accretion efficiency, and M_7 is the total SMBHB mass in units of $10^7 M_{\odot}$. We follow [40] and use a typical value of $\epsilon = 0.1$.

2.3.2 Peak accretion luminosity from magnetohydrodynamic simulations

The second peak luminosity estimate we utilise is described in [38]. This study employs several magnetohydrodynamic simulations of merging SMBHBs in gaseous environments like AGN disks, for different initial binary characteristics and configurations. Where the study itself is too detailed for our purposes, the authors derived a rather simple expression for the peak luminosity, which is also accretion-powered. They found that, over a large range of initial values, the gas flow regulates the EM luminosity. The peak luminosity at merger can be approximated with

$$L_{\text{acc, MHD}} \approx 1.2 * 10^{46} \rho_{-13} M_8 \text{ergs s}^{-1}, \quad (21)$$

where ρ_{-13} is the gas density around the merging SMBHB in units of 10^{-13} g/cm^3 . We use the typical value of $\rho_{-13} = 1$. It should be noted that while both models predict an accretion-powered luminosity, their derivations are slightly different. On the one hand, [40] finds an estimate through analytical means, by making certain simplifying assumptions about the SMBHB setup. On the other hand, [38] reports an order-of-magnitude luminosity by noticing similarities in peak luminosity among numerical simulations with different binary configurations.

3 Results and discussion

In this section, we will show the results that our frameworks can generate, and discuss them and their validity accordingly. Specifically, we will focus on the GRB and KN model, as these are the most important models in this project. The EM signatures of BBHs and SMBHBs will not be discussed; after all, these models are merely theoretical order-of-magnitude estimates. Additionally, EM counterparts to any of these two types of GW events have not been detected yet, so comparison with observations would not be possible. Concerning the GRB model, we will first highlight its general characteristics by discussing the lightcurves for different setups. Subsequently, we will confront our GRB simulation with observations on GRB170817A. We will make this comparison by plugging in and justifying a set of typical values for our free parameters, after which we make a verdict on the validity of our GRB model. We will discuss the KN model by making comparisons with the observed lightcurve of AT2017gfo. After this, we will briefly highlight the results from our luminosity estimates of stellar-mass and supermassive black hole binaries. Finally, at the end of this Section, we will illustrate the merits of including EM counterparts to the Toolbox. We will use the Toolbox to simulate a universe with BNS mergers, after which it will return a catalogue with the properties of all BNSs that will be observed by a selected GW detector. For a chosen high energy detector (satellite), we will use our models to predict for which of these will have detectable GRB counterparts. We will graphically show the characteristics of all events with joint observations.

3.1 Short gamma-ray bursts

3.1.1 General characteristics of the model

Here, we will discuss the general working of the sGRB model that we employ. Fig. 11 shows the general trends of the photon flux νF_ν as a function of time. We evaluate the flux at a frequency $\nu \approx 2 \times 10^{19} \text{Hz}$, and $\Delta\theta = 0.05$. Specifically, we can see the dependence of the observed flux on the viewing angle θ_v . In the following, we will discuss the shapes of these curves by highlighting the main concepts that make up the GRB flux: time lag, the area of the emitting region, and the relativistic beaming effect.

3 Results and discussion

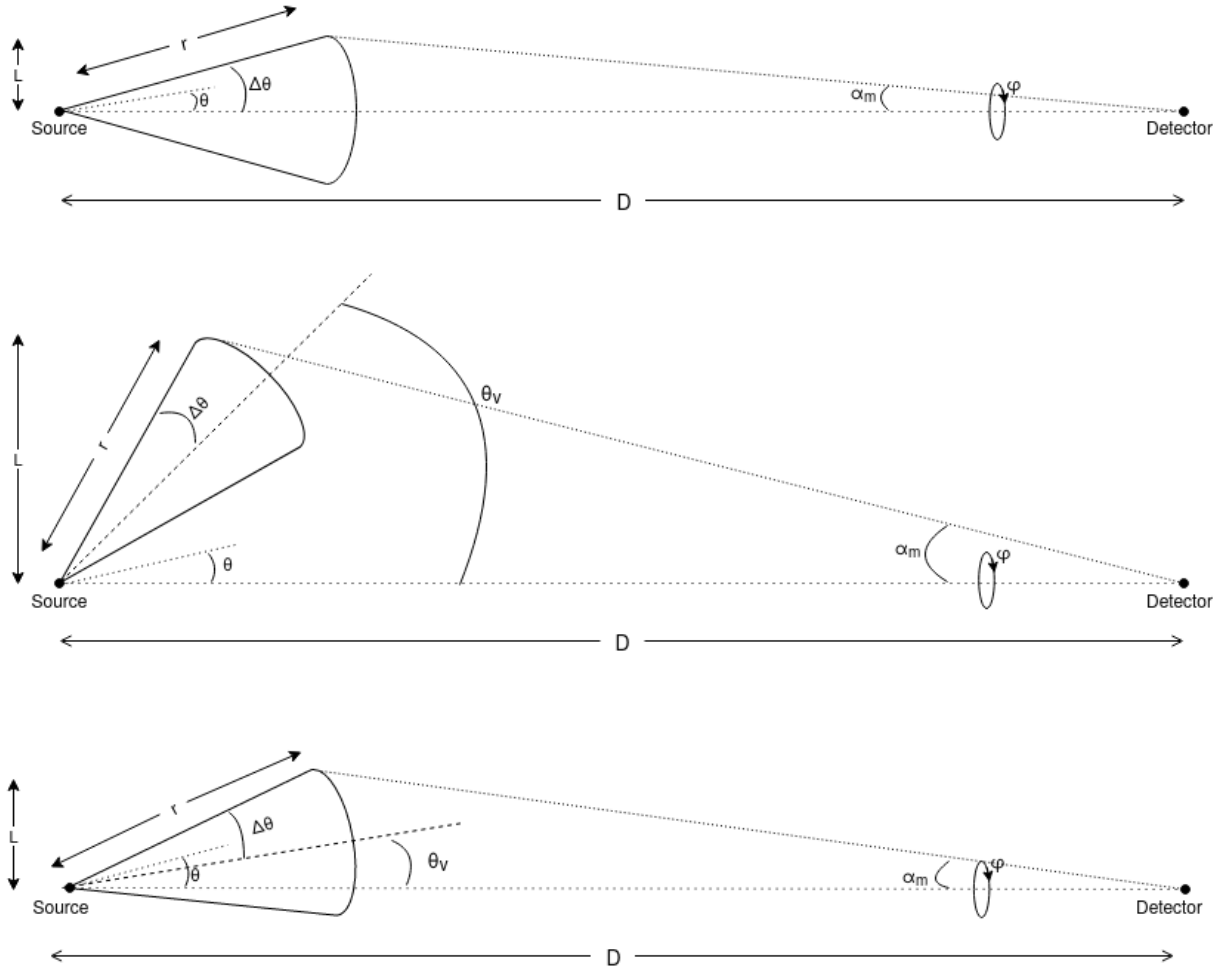


Figure 10: We include once again the general setup of our jet structure model that produces the sGRB. Bottom panel: face-on view, i.e. a θ_v of 0. Middle panel: $\theta_v > \Delta\theta$, so we are outside of the GRB beam. Bottom panel: $\theta_v < \Delta\theta$, i.e. we find ourselves within the beam. Drawings are inspired by [65].

The first aspect, the time lag, is clearly visible in Fig. 11, especially for the $\theta_v = 0.2$ case. By ‘time lag’, we mean the fact that the observed GRB emission is delayed with respect to $T = 0$, which is the time when the peak GW signal arrives on earth. We observe that the $\theta_v = 0.2$ setup is delayed by about $\sim 2s$ with respect to $T = 0$. It is important to note that, even though hardly visible here, there is certainly also a time lag for the other two setups ($\theta_v = 0$ and $\theta_v = 0.05$). These curves start at $T \approx 0.02s$. We distinguish two types of time lag. The first type results from the *difference in propagation speed* between the GWs and the jet. To visualise this, here, we include Fig. 10, which is the same as Fig. 6. This type of delay is dominant in the case for $\theta_v = 0$ (cf. the top panel in Fig. 10), and for $\theta_v = 0.05$ (bottom panel in Fig. 10). Both of these setups are so-called ‘on-axis’ scenarios, which means that the line-of-sight is inside the cone. At

the time of merger, at $t = 0$ in the source frame, the peak GW signal leaves the system from the origin and propagates towards us at the speed of light c . At the same time, i.e. also starting at $t = 0$, the jet propagates at a speed βc towards us, until it reaches r_0 , where the sGRB occurs. In other words, when the sGRB happens at r_0 , the GW signal has already travelled further due to the slower speed of the jet. The photons emitted at r_0 during the sGRB will therefore always arrive *after* the GW signal. The corresponding delay time between the peak GW signal and start of the sGRB is $T_{d,j} = r_0(1/\beta - 1)/c$. A second type of time delay, which becomes dominant only at higher viewing angles (in Fig. 11 for $\theta_v = 0.2$, middle panel of Fig. 10), is the *geometric time delay*. This type arises when the *first* gamma-radiation that reaches the detector is not in the line-of-sight, but rather off-axis, i.e. when $\theta_v > \Delta\theta$. In Fig. 10, this would be the radiation released from an angle $\theta = \theta_v - \Delta\theta$. This off-axis radiation reaches the detector later than emission that would have been released from the line-of sight (i.e. from $\theta = 0$) at the same time. This is easier to imagine with the help of the middle panel in Fig. 10. Compare the location $(r, \theta) = (r_0, 0)$ with $(r, \theta) = (r_0, \theta_v - \Delta\theta)$: the distance between the former and the observer is smaller than between the latter and the observer. As such, photons emitted from (r_0, θ) will have a longer travel path, and their arrival time will therefore be delayed as compared to photons from r_0 in the line-of-sight. This time delay can be described by $T_{d,g} = (1 - \cos(\theta_v - \Delta\theta))r_0/c$. From here, we can clearly see that the geometric time delay goes up with increasing θ_v . It should be noted that in this scenario, the jet propagation speed time delay is also present, but simply plays a much smaller role than the geometrical time delay. For on-axis setups like the top and bottom panel in Fig. 10, the geometrical time delay does not play a role, as the first emission in these cases will be from the line-of-sight. We can infer a general expression that describes the starting time of the GRB with respect to $T = 0$, taking into account both types of time lag:

$$T_{\text{start}} = \frac{r_0}{c\beta} [1 - \beta \cos(\max[0, \theta_v - \Delta\theta])]. \quad (22)$$

The GRB starting times in Fig. 11 are all in line with Eq. 22.

Next, we will discuss the role of the area of the emitting region on the flux curve. To explain this, we introduce two very important quantities: $\theta(T)$, which is the polar angle of the emitting region at instant T, and $\Delta\phi(T)$, which is the azimuthal angle range of the emitting region, also at instant T. We will explain both of these individually, after which we can highlight the important role of the area of the emitting region. In Fig. 14, we plot $\theta(T)$ as a function of time, according to

$$\theta(T) = \cos^{-1} \left(1 - \frac{cT}{r_0} \right). \quad (23)$$

First of all, it should be noted that $\theta(T)$ is shifted in time, i.e. it does not start exactly at $T = 0$, but at $T = T_{d,j} \approx 0.02s$ due to the first type of time delay we discussed. We observe in Fig. 14 that $\theta(T)$ increases for higher T , i.e. emission released from higher θ

3 Results and discussion

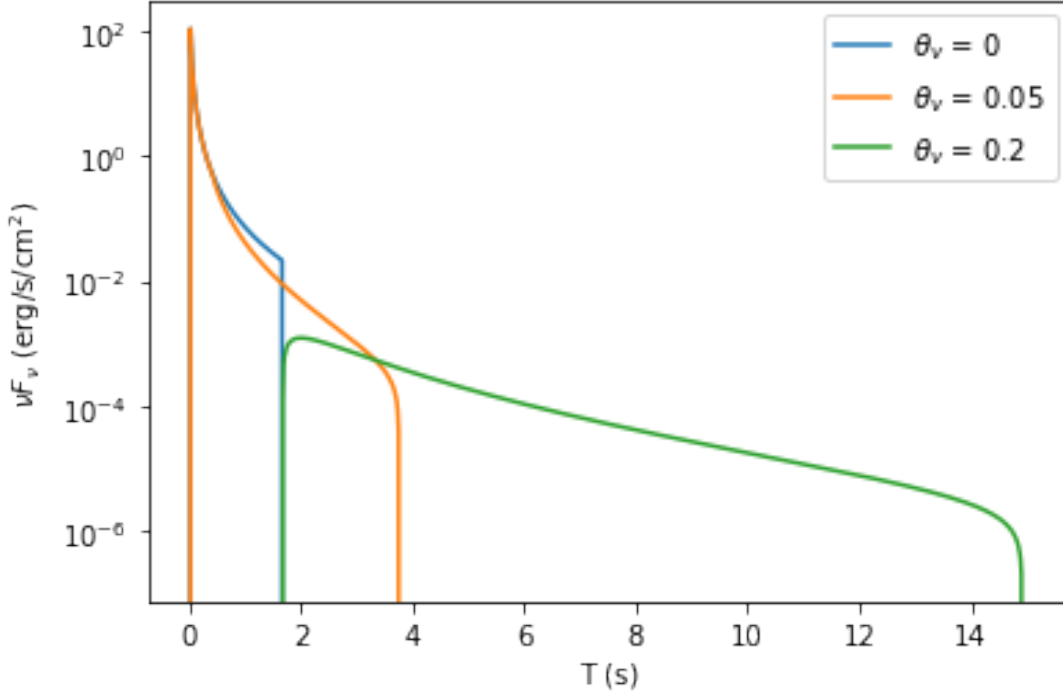


Figure 11: Evolution of the GRB flux νF_ν , as a function of time. We evaluate the flux at $\nu = \nu'_0 \approx 2 \times 10^{19} \text{Hz}$ and plot for three different viewing angles θ_v . We employ $\Delta\theta = 0.1$, $\gamma = 100$, $E_{GRB} = 5 \times 10^{50} \text{ergs}$, and $D = 40 \text{Mpc}$. Please note that we do not discuss the physicality of these values here; they merely serve as input for our model, so we can show the general trends and structure of the GRB flux curve.

will be received at later times. This corroborates with the setup in any of the panels in Fig. 10; the radiation, emitted from r_0 , needs to travel a larger distance when it is sent off towards us from a higher angle θ . We receive photons that need to cover a smaller distance first. These are the photons that originate from lower θ . From this conceptual understanding of the temporal evolution of $\theta(T)$, we jump to the azimuthal angle range of the emitting region, $\Delta\phi(T)$. In our breakdown of this quantity, we will be assisted by Fig 12, which shows a schematic picture of the observer view, for the three different viewing angles $\theta_v = 0$ (left), $\theta_v = 0.05$ (middle), and $\theta_v = 0.2$ (right). From left to right, these three front views correspond to respectively the top, bottom, and middle panel in Fig. 10. The dot in each panel represents the direction of our line-of-sight. Let us start this explanation by investigating the left panel in Fig. 12, because the $\theta_v = 0$ case is the simplest setup. In this scenario, we, as observers, are exactly in the middle of the cone. The first radiation we receive will be exactly from the line-of-sight (i.e. $\theta(T) = 0$). Then, we observe photons emitted from higher angles θ . All radiation we see at some instant T originates from a ring region, which is plotted as a dotted circle in Fig. 12. This ring gets larger and larger as time goes on and photons from larger θ receive our detector. Now, $\Delta\phi(T)$ is the angle range that this ring covers at some time T . For the $\theta_v = 0$ case,

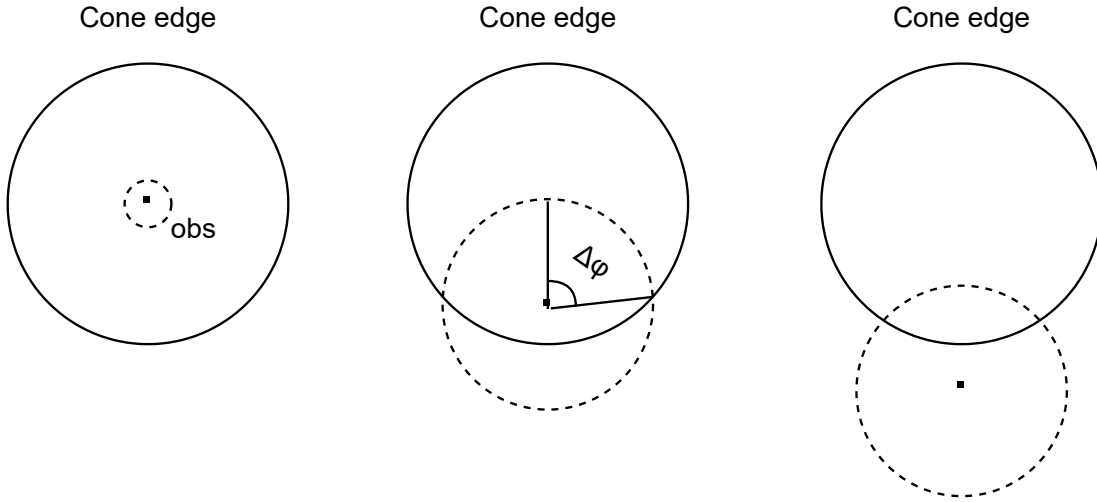


Figure 12: Observer view of the sGRB emission region, for three different setups: $\theta_v = 0$ (left), which corresponds to the top panel in Fig. 10, $\theta_v = 0.5$ (middle), which corresponds to the bottom panel in Fig. 10, and $\theta_v = 0.2$ (right), which is the same setup as the middle panel in Fig. 10. Each of the three images represents a snapshot in the GRB pulse at some time T . The dotted circles correspond to all the points that reach the detector at the same time in their particular setup. We introduce the angle $\Delta\phi(T)$ to account for the fact that in some setups (middle and right), at some T -range, only part of the dotted circle lies within the cone.

the emitting region at time T is always a full ring, so $\Delta\phi(T)$ is always π . Please note that we assume spherical symmetry here, so we can simply put a factor 2 in front of $F_\nu(T)$ and take $\Delta\phi(T) = \pi$, rather than setting it to 2π . However, for a non-zero viewing angle, e.g. the middle panel in Fig. 12 corresponding to $\theta_v = 0.5$, $\Delta\phi(T)$ is not always π . In this panel, our line-of-sight, is still inside the cone, but not exactly in the middle anymore. Also here, as θ increases, the ring size increases. However, at some point in time (i.e. from some $\theta(T)$ onwards), not all points on this ring will lie within the cone anymore. This is visible in the middle panel; the dotted circle once again represents the ring of emission points with equal θ , at some instant T . Clearly, only approximately half of the ring lies within the cone at this T . In this scenario, the corresponding angle of the emission region is not π anymore, but a more complex expression:

$$\Delta\phi(T) = \cos^{-1} \left(\frac{\cos \Delta\theta - \cos \theta(T) \cos \theta_v}{\sin \theta_v \sin \theta(T)} \right). \quad (24)$$

In the far right panel of Fig. 12, which depicts the off-axis scenario of $\theta_v = 0.2$ (middle panel in Fig. 10), $\Delta\phi$ is never π , i.e. it is always described by Eq. 24. At every instant in time, only part of the ring lies within the cone. A nice side note: from this front view: we can clearly see the geometrical time delay. In this setup, the first radiation we receive is not from the line-of-sight, but from the bottom edge of the cone. From $T = 0$ onwards, the size of the ring at each $\theta(T)$ grows. Still, during the first few moments, the ring is too small and does not reach the edge of the cone. Then, only after some considerable

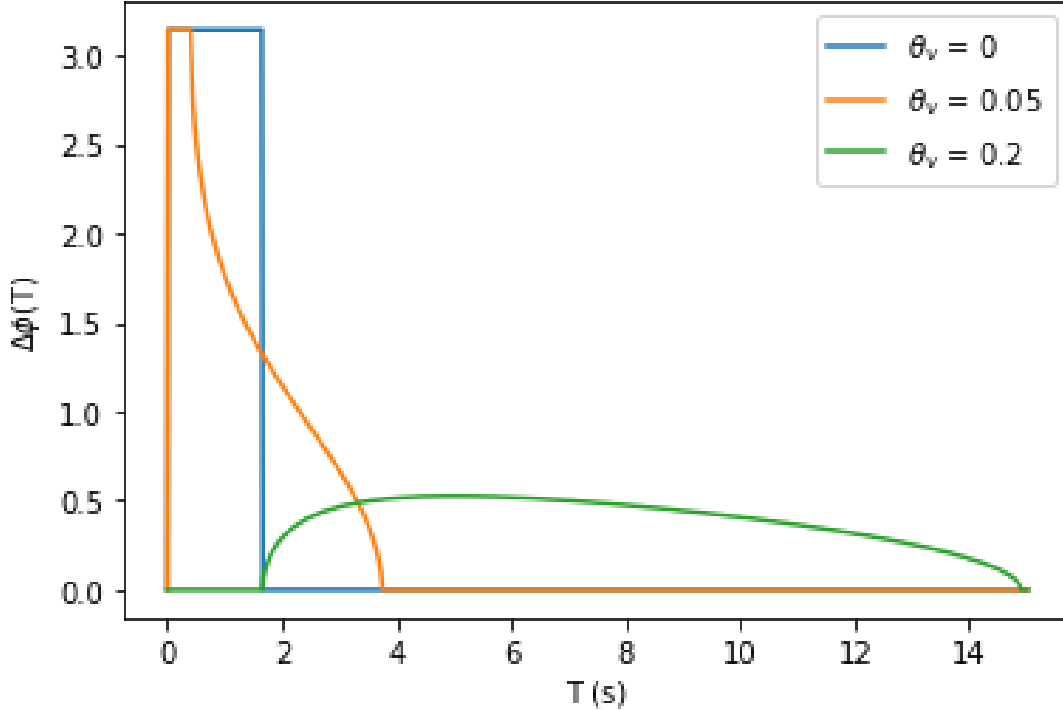


Figure 13: $\Delta\phi(T)$ for three different viewing angles, as a function of time. NB: the area under each curve is the same (around 0.52 in this case); the total emission region is the same in all cases. $\Delta\phi(T)$ simply describes how it is distributed over time.

amount of time, the ring is large enough that it touches the cone edge, which is when we see the first radiation. The geometrical time lag would be the time between $\theta(T) = 0$ and the moment when the growing ring touches the cone for the first time.

In Fig. 13, we plot the temporal evolution of $\Delta\phi(T)$, for all three different viewing angles. Indeed, this plot reflects the main characteristics of each $\Delta\phi(T)$ that we discussed. For $\theta_v = 0$, we observe that $\Delta\phi(T)$ is always π . In the $\theta_v = 0.05$ case, we see that $\Delta\phi(T)$ initially remains π , but as the ring touches the cone edge after which $\Delta\phi(T)$ is described by Eq. 24 and the emission area goes down quite rapidly. In the scenario where $\theta_v = 0.2$, where $\Delta\phi(T)$ is fully described by Eq. 24, we first see a steady increase in $\Delta\phi(T)$, after which a gradual decline happens. In this scenario, the emission is much more spread out over time and does not show peaks that are as high as in the other two cases.

The curves we see in Fig. 13 are extremely important for the overall lightcurves that are visible in Fig. 11. Where the exponential decay that we see for each graph in Fig. 11 can be explained by the relativistic beaming that we will explicate in the next paragraph, the fast initial rise in flux for all curves in the same figure is a direct result of $\Delta\phi(T)$. It should be noted that the step rise - exponential decay combination is typical for sGRBs [34], but the rise looks to be instant, which may deviate slightly from

typical GRB spectra. We can draw a parallel between the sudden increase in all curves of Fig. 11, and those in Fig. 13. We explain this behaviour for the case $\theta_v = 0$ first. We once again refer to the left panel of Fig. 12. Additionally, also here, Fig. 14, where we depict $\theta(T)$ as a function of time (according to Eq. 23), plays an important role. $\theta(T)$ influences $\Delta\phi(T)$ as in Eq. 24, which in turn is important in Eq. 14. In Fig. 14, $\theta(T)$ starts to exist at $T = T_{d,j} = T_{\text{start}}$, which is $\sim 0.02\text{s}$ here, as a result of the jet propagation speed time lag. At this very first instant, $\theta(T) = 0$. The area of the emitting ring that increases in size is dependent on $\theta(T)$ (it is proportional to $\sin\theta(T)$). At $T = T_{d,j}$, i.e. then $\theta(T) = 0$, this area is 0, i.e. the ring does not exist yet. Therefore, at $T = T_{d,j}$, the flux is 0. The emitting ring only starts to exist some infinitesimally small amount of time later, at $T = \epsilon$. At this point, $\theta(\epsilon)$ is non-zero, which results in a non-zero $\Delta\phi(\epsilon)$ that produces the first detected flux. We observe that Fig. 14 is the steepest the instant after $T = 0$; this very sharp increase in $\theta(T)$ at the instant $T = \epsilon$ generates the extremely steep rise that we see in all spectra of Fig. 11. All of the energy that is generally divide over a more smooth increase in GRB flux curves (see e.g. [3]) is, in our model, all contained in the very first timestep after $T = T_{d,j}$. For the off-axis case, this still holds, however in a slightly different fashion. In that scenario, depicted on the right panel of Fig. 12, the ring first increases in size without resulting in any flux, due to the fact that the line of sight lies outside the cone. At the instant when $\theta(T)$ touches the jet edge (i.e. when $\theta(T) = \theta_v - \Delta\theta$), $\Delta\phi(T)$ starts to exist. Since our jet edge is a hard boundary rather than a gradual one, also here we see a steep increase in flux, as visible in Fig. 11. In our model, all of the energy that is generally divide over a more smooth increase in GRB flux curves (see e.g. [3]) is all contained in the very first timestep. We do not deem this problematic, as it should still generate the same total amount of flux. Still, if one wishes to make the rise more gradual, one could adopt a more realistic distribution for the internal shock location r_0 , that we set as a Dirac delta distribution in this project. Using e.g. a Gaussian distribution around r_0 would generate many individual instant-rise curves like these, which, when added together, would produce a curve that overall has a smoother rise.

The third main ingredient that makes the flux curves as we observe them in Fig. 11 is the concept of *relativistic beaming*. The photon flux, originating from the jet, appears concentrated in the line-of-sight: it is "beamed". The majority of the flux is contained within an angle of $\sim 1/\gamma$ away from the line-of-sight. In Eq. 14, this concept is captured by the factor of $1/(\gamma^2[1 - \beta \cos\theta(T)])^2$. To illustrate this, let us take the $\theta_v = 0$ case as an example. For good visualisation, we once again refer to the left panel in Fig. 12. Because of the relativistic beaming, the bulk of the flux is concentrated in the region up to $\theta \approx 1/\gamma \approx 0.01$ for $\gamma = 100$. As the emitting ring grows over time, it passes the $\theta = 0.01$ mark very soon, beyond which the measured flux drastically decreases. In other words, as the ring moves away from the beaming lobe, the flux decays exponentially. This is clearly visible in Fig. 11 specifically for the $\theta_v = 0$ case (blue) we use here, but also for the other two viewing angles. We can see that the decay is significantly less steep for the highest viewing angle. This can be attributed to the fact that the increase in $\theta(T)$ is steepest for low T ; this can be very clearly seen in Fig. 14. As a result, the beaming factor $1/(\gamma^2[1 - \beta \cos\theta(T)])^2$ results in steeper decreases for low $\theta(T)$. Given the fact

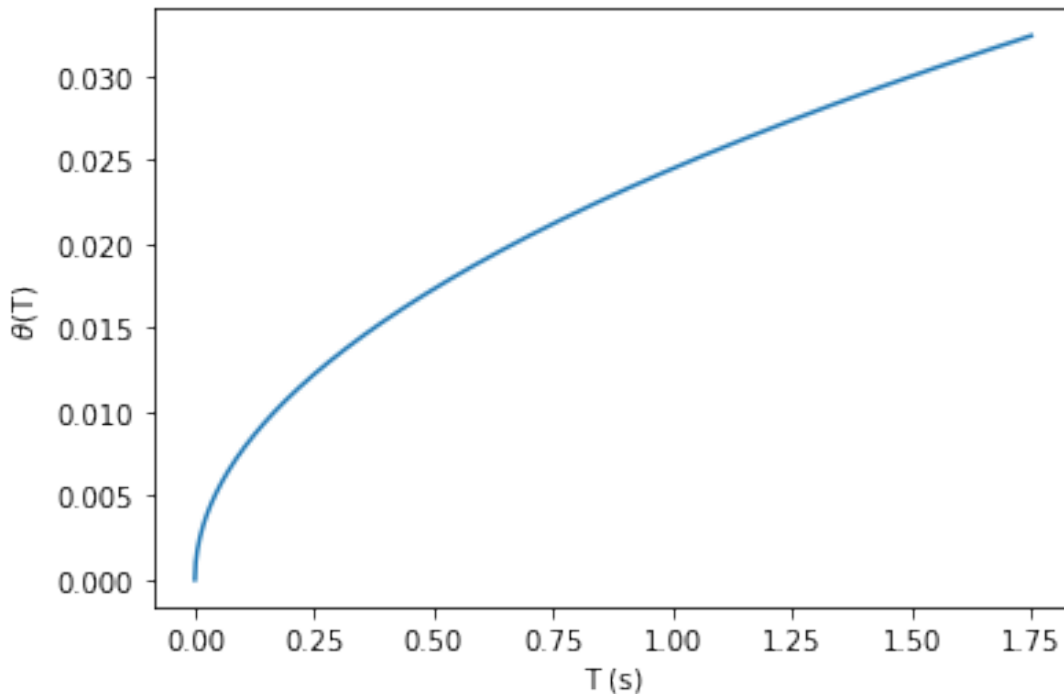


Figure 14: $\theta(T)$ according to $\cos^{-1}(1 - Tc/r_0)$.

that we only observe radiation from the $\theta_v = 0.2$ scenario from higher $\theta(T)$ onwards, the decay is less steep there. The relativistic beaming can explain why the peak flux (see Fig. 11 for the off-axis case ($\theta_v = 0.2$)) is significantly lower than for the two on-axis cases. Radiation from the latter two is seen in the line-of-sight, where the beaming makes for a highly concentrated peak flux.

3.1.2 Comparison with GRB170817A

To test the validity of our model, it is important that we compare it to sGRB observations, especially to those that have a BNS as confirmed origin. As we know, with GRB170817A [26], we only have one such event. Therefore, in this section, we will compare the characteristics of our model to the observables of GRB170817A. In order to predict the GRB observables, we need to insert typical values for our free parameters ($\Delta\theta, \theta_v, r_0, \gamma, \nu'_0$ and E_{GRB}) that correspond to the properties of GRB170817A. Even though some of these can be directly inferred from the GW and EM observations, still quite large uncertainties exist. We will here provide the choices for our parameters, after which we will compute several observables of GRB170817A. For each observable, we will argue how well our calculation fits with values found in GRB170817A. Then, we will discuss the validity of the parameters we insert; we will investigate and report whether the values we use are typical for GRBs, and whether this is a result of GRB170817A being an atypical GRB or whether our model shows limitations and over-

3 Results and discussion

Table 1: An overview of the values for sGRB parameters that we insert into our model.

$\Delta\theta(^{\circ})$	$\theta_v(^{\circ})$	r_0 (cm)	γ	ν'_0 (Hz)	E_{GRB} (ergs)	D (Mpc)
24	29.9	10^{13}	275	10^{19}	10^{49}	40

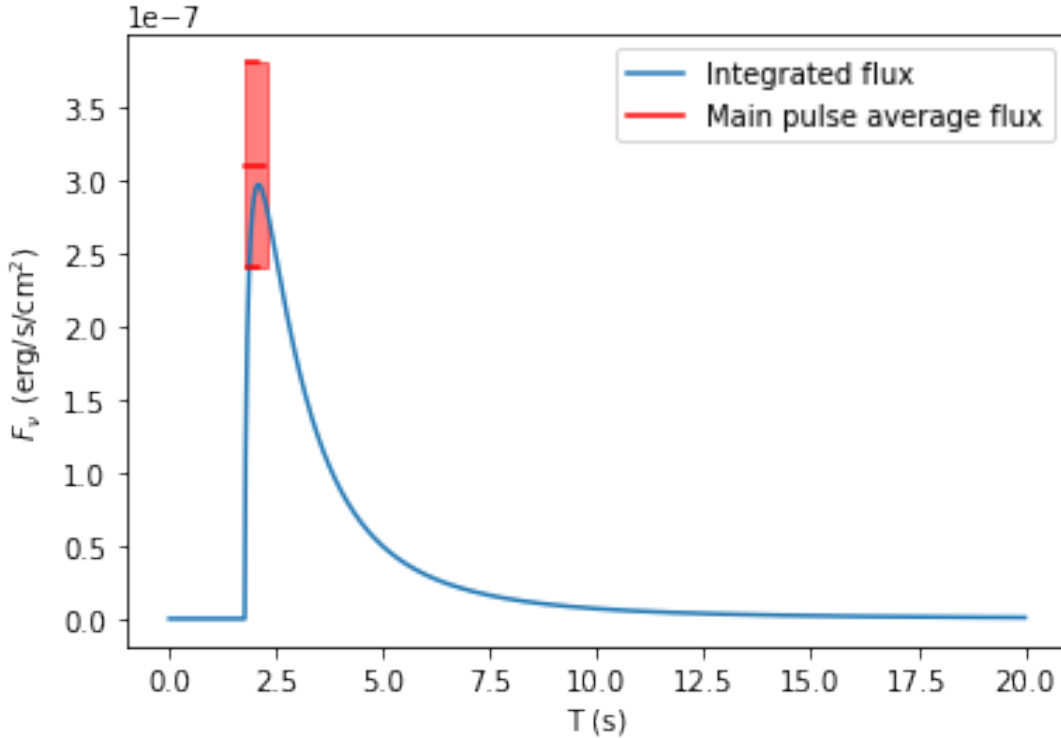


Figure 15: Temporal evolution of the flux, integrated over the 10-1000 keV energy band. We also show the average flux during the main peak that has been computed from observations, out to ~ 0.5 s after T_{start} [3].

simplifications. In Table 1, we list all values for the model parameters that we employ.

In Fig. 15, we show the temporal evolution of the flux, integrated over the standard 10-1000 keV photon energy band. This figure allows us to investigate several things. First of all, we look at the general shape of this curve. Indeed, we can conclude that this recovers the typical GRB shape quite well; we see a fast rise followed by an slower exponential decay. It should be noted that the sGRB detection in [26] does not contain any observations of the energy flux, but rather the photon counts in some time bin. Conversion between these two quantities is very cumbersome, and more importantly, introduces additional uncertainties. Therefore, we are not able to compare our model with GRB170817A in this regard. Still, [26] reports an average flux of the main peak (up to ~ 0.5 s after T_{start}) of 3.1 ± 0.7 ergs $\text{s}^{-1} \text{cm}^{-2}$. We include this in Fig. 15, from which we can see that our model complies with it within the error range. [3] reports

3 Results and discussion

$T_{90} = 2.0 \pm 0.5\text{s}$, which is the interval over which 90% of the burst fluence (ergs/cm^2) is accumulated in the energy range of 50-300 keV (i.e., the bulk of the GRB pulse duration). In Fig. 15, we can observe that the main pulse in our model also lasts $\sim 2\text{s}$. Therefore, we can state that we are able to recover the GRB duration quite well with this simplified model. Additionally, we can infer T_{start} from our definition in Eq. 22. [26, 3] report a $T_{\text{start}} = 1.734 \pm 0.054\text{s}$. With our model, we obtain $T_{\text{start}} = 1.768\text{s}$. This falls nicely within the range of the detected value. Additionally, we here report the fluence that we obtain with our sGRB model. Within the 10-1000 keV range and over an interval of $[T_{\text{start}}, T_{\text{start}}+2]$, our model gives a fluence of $2.69 \times 10^{-7} \text{ ergs cm}^{-2}$, which we may compare to the $2.8 \pm 0.2 \times 10^{-7} \text{ ergs cm}^{-2}$ from the observations. Also this is a good prediction of this particular observable.

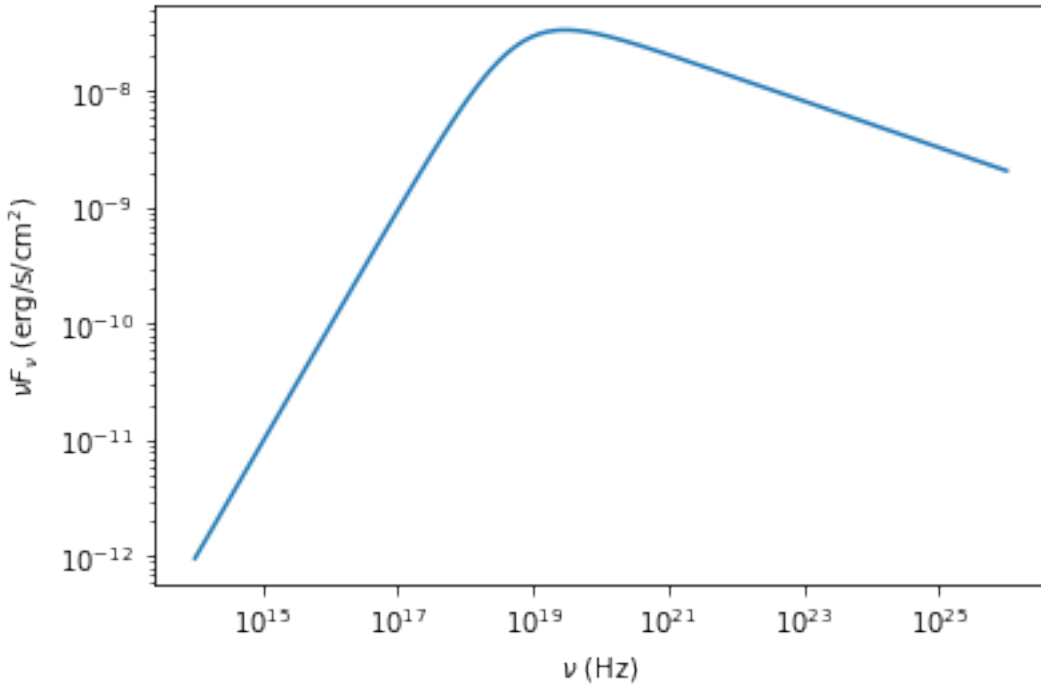


Figure 16: Spectrum of the time-integrated νF_ν , as a function of photon frequency ν . As integration range, we used $[T_{\text{start}}, T_{\text{start}}+2]$.

We also compute the time-integrated spectrum, in which we integrate νF_ν over the range $[T_{\text{start}}, T_{\text{start}}+2]$. We show this result in Fig. 16. We define E_{peak} as the photon energy that corresponds to the peak νF_ν in this graph. With our model parameters, we get $E_{\text{peak}} \approx 118 \text{ keV}$. This is a bit lower than the E_{peak} of $\sim 185 \text{ keV}$ reported in [26], but still of the same order of magnitude.

We have seen that the observables and GRB shape are recovered well with the input values for the free parameters that we specify in Table 1. In the remainder of this Section, we will discuss whether the values we used in Table 1 are actually typical for sGRBs, and what that means for the predictive capabilities of our sGRB model.

First, we will discuss $\Delta\theta$ and θ_v , for which we respectively use 24° and 29.9° . Concerning $\Delta\theta$, we refer to [23]. This study presents a comprehensive catalogue of afterglow observations from all sGRBs between November 2004 and March 2015 of which afterglow detections were done. Using afterglow data from 11 of the events in this catalogue, the authors found a median opening angle of the GRB jet of $16 \pm 10^\circ (1\sigma)$. As such, given that the $\Delta\theta$ we use lies well within this range, we can assume that this is a typical value for this particular parameter. From the GW observations in [4], the viewing angle, θ_v , was constrained to be $\leq 32^\circ$. We can therefore also conclude that our choice for θ_v is compatible with those constraints from observations, for it lies within this (albeit rather large) range. Also our choice for r_0 can be justified. Review article [9] reports that the internal dissipation of relativistic jet energy happens at $r_0 \approx 10^{13} - 10^{16}$ cm. Where numerous uncertainties still exist, our choice certainly seems typical as it falls within this range. The Lorentz factor γ be restricted through theoretical conditions. In order to have a physical setup, one needs to avoid the compactness problem in sGRBs (see [55, 57]). The requirement to solve this problem is that the source moves relativistically towards the observer with $\gamma \geq 100$. With our γ , we fulfill this requirement and therefore use a typical GRB Lorentz factor. For the typical frequency in the comoving frame, ν'_0 , we have to refer back to our spectrum in Eq. 8. By using this equation, we emulate the Band spectrum [10] that is based on observed GRBs. This is a broken power law with an exponential cutoff, where the break happens at ν'_0 . By choosing $\nu'_0 = 10^{19}$ Hz, in combination with a $\gamma \approx 10^2$, the spectrum in the observer frame breaks at a corresponding energy of ~ 10 - 100 keV. This is typical for sGRBs [10]. Additionally, [33] reports that the choice for ν'_0 does not matter so much, as long as it is included in the detector sensitivity range. That is the case for this ν'_0 . The value $D = 40$ Mpc corresponds with both GW and EM observations [4, 26].

Where all aforementioned values seem typical for GRBs and therefore sensible, our $E_{GRB} = 10^{49}$ ergs seems off as compared to standard values. It is quite low, as compared to the distribution for the typical beaming-corrected GRB energy, as reported in [24]. This 2001 study found that the total energy release of all sGRBs with known redshifts at that time could be approximated by a Gaussian distribution around 5×10^{50} ergs, with a 1σ multiplicative factor of 2. This does, however, not mean that our E_{GRB} is faulty. First of all, the distribution in [24] may be inaccurate. As the GRB sample is quite small ($N = 17$) and the study is ~ 20 years old, updates to this distribution with all currently known sGRBs may include the energy output of GRB170817A. Additionally, observation biases leading to less detections of low-energy GRBs can play a role here. Next to this, [3, 26] report that GRB170817A is intrinsically dim as compared to usual measures. Therefore, the E_{GRB} we use may be atypical, but it is certainly not unphysical.

Given the fact that our model seems to recover GRB170817A well with sensible input values, our final verdict is that we deem it acceptable and reasonable. Definitely for a first version in the Toolbox, its performance is solid. Still, it is good to mention where potential improvements could be made. First of all, even though it is a very good approximation, the top-hat jet structure is slightly unrealistic. If one were to improve the model, one could introduce a smoothly increasing jet velocity profile at the edges,

to get rid of the hard-cut jet rim. The same could be done for the location of the internal shock, which would make the rise in Fig. 11 more gradual. Moreover, where both γ and ν'_0 are currently taken as constants, they are generally parameters that depend on the geometry of the setup. In fact, the authors of [34] are aware of this; in a recent study [35], a new, more complex jet structure is suggested. In this update, γ and ν'_0 (and therefore the spectrum) have an angular dependence, i.e. $\gamma(\theta)$ and $\nu'_0(\theta)$. For details of this structure, we refer the reader to [35]. This update could be implemented in future versions of the GW Toolbox.

3.2 Kilonovae

The KN model we employ works differently than the GRB mathematical framework, in the sense that it is not an analytical formula with which one can easily show properties of the model, after inserting typical values for some free parameters. As was explained in Section 2.1.3, the KN model merely operates in an input-output fashion: binary properties as input, the lightcurve and bolometric luminosity in different bands as output. As such, giving an extremely detailed analysis of the general characteristics we did in the GRB case does not apply here. Instead, we will do the following: first, in the paragraph below, we will provide the input values that we will insert into our model. These will correspond to the properties of GW170817. Then, in the next subsection, we will show the KN lightcurves that we are able to generate with these input values, in different photometric filters. While depicting these results, we will illustrate and discuss the general outcome of the model; we will link the lightcurves to typical KN characteristics. After that, we will compare the lightcurves to observations of AT2017gfo. We will do the same for the bolometric luminosity that the model can compute. Finally, we will give a verdict on the accuracy of our model.

In Section 2.1.3, we provided an overview of the working of our KN model, including the input parameters one has to insert (see Fig. 8): m_1, m_2 (i.e. the NS masses, with $m_1 \geq m_2$), and the NS EOS. Now, in fact, the model allows for additional parameters, which we did not mention for the sake of simplicity. One of these that we will use here (and in the Toolbox) is the effective spin $\chi_{\text{eff}} = (m_1\chi_1 + m_2\chi_2)/(m_1 + m_2)$, where χ_1 and χ_2 are the individual NS spins. The reason why we utilise this extra parameter is the fact that the Toolbox can give this as output. As such, we use 4 input parameters: m_1, m_2, EOS , and χ_{eff} . In choosing these, we follow [61]. From gravitational waveform templates, the authors find the following distributions for the properties of GW170817: $m_{\text{chirp}} = 1.198_{-0.001}^{+0.001} M_{\odot}$ ⁴, $q = 0.756_{-0.157}^{+0.068}$ ⁵, and $\chi_{\text{eff}} = 0.029_{-0.018}^{+0.017}$. From these, we infer our input values, which we list in Table 2. The EOS we use ('H4') is the standard EOS in `gwemlightcurves`.

⁴ $m_{\text{chirp}} = (m_1 m_2)^{3/5} / (m_1 + m_2)^{1/5}$.

⁵ $q = m_2 / m_1$.

Table 2: Input parameters for our KN model that functions to emulate AT2017gfo.

$m_1(M_\odot)$	$m_2(M_\odot)$	χ_{eff}	EOS
1.5858	1.1989	0.029	'H4'

3.2.1 General KN characteristics and outcome of the model

In Fig. 17, we see the main output of our model, where the absolute magnitude in 9 different passbands is depicted. From here, we can clearly see several typical KN characteristics. One of these is visible in the in the NIR bands: J , K and H (red/orange). Emission in these three bands, showing a similar shape, is clearly a result of the "red" KN. As mentioned in Section 2.1.3, decaying lanthanide-bearing tidal ejecta release photons mainly in the NIR part of the EM spectrum. These ejecta typically arise after several days - something that is visible here as well, as these curves do not reach their peak before 2-3 days after $t = 0$ d. Not only does emission from these bands generally arise later, it also lasts longer [22]. This is also the case in this image; especially the K band persists until ~ 15 days after the $t = 0$ d. More wavebands that show similar behaviour amongst each other are the g , r , and i bands. These curves peak immediately, then subsequently decay. They are initially brighter than the "red" KN; this is in accordance with typical KN lightcurves. These mainly originate from the "blue" KN: lanthanide-free ejecta release radiation in the visible part of the spectrum. Two of the bands that we have not touched upon, the z and y bands, cover wavelengths that lie between the J , K , H and g , r , i bands. Situated in the low-NIR region, it makes sense that their resulting emission is a result from a combination of the "blue" and "red" KN. We observe a shape similar to the high-NIR bands (initial steady rise peaking at $t \approx 2 - 3$ d, slow decay), yet slightly brighter due to the added radiation from the lanthanide-free ejecta of the "blue" KN. The u band, in the UV part of the spectrum, only has a small contribution in typical KN, which we can see is also the case here. Also the magnitudes we observe are typical; KN lightcurves generally show absolute magnitudes up to ~ -16 . The duration of the two main EM signals is typical as well. The "blue" KN may last up to several days, while red lasts weeks. Finally, we see that all lightcurves become dimmer with time. Needless to say, this is in accordance with typical KNe, as the amount of decaying elements that release photons observed in the KN is limited; as time goes on, less decaying elements are present, so less EM radiation is released [46, 22, 9]. Overall, therefore, we can conclude that this figure recovers the typical KN spectrum quite well. Additionally, we report the ejecta mass and velocity from our initial values: respectively $\sim 0.03M_\odot$ and $\sim 0.2c$. These fall nicely within a typical range of $m_{\text{ej}} \in [10^{-2}, 10^{-1}]M_\odot$ and $v_{\text{ej}} \in [0.2c, 0.3c]$ [36].

3.2.2 Comparison with AT2017gfo

Fig. 18 shows the resulting lightcurve of the specified input values for m_1 , m_2 , and χ_{eff} , this time compared to a set of AT2017gfo observations [60]. The dotted line represents the lightcurve resulting from the input parameters we used. It should be noted that

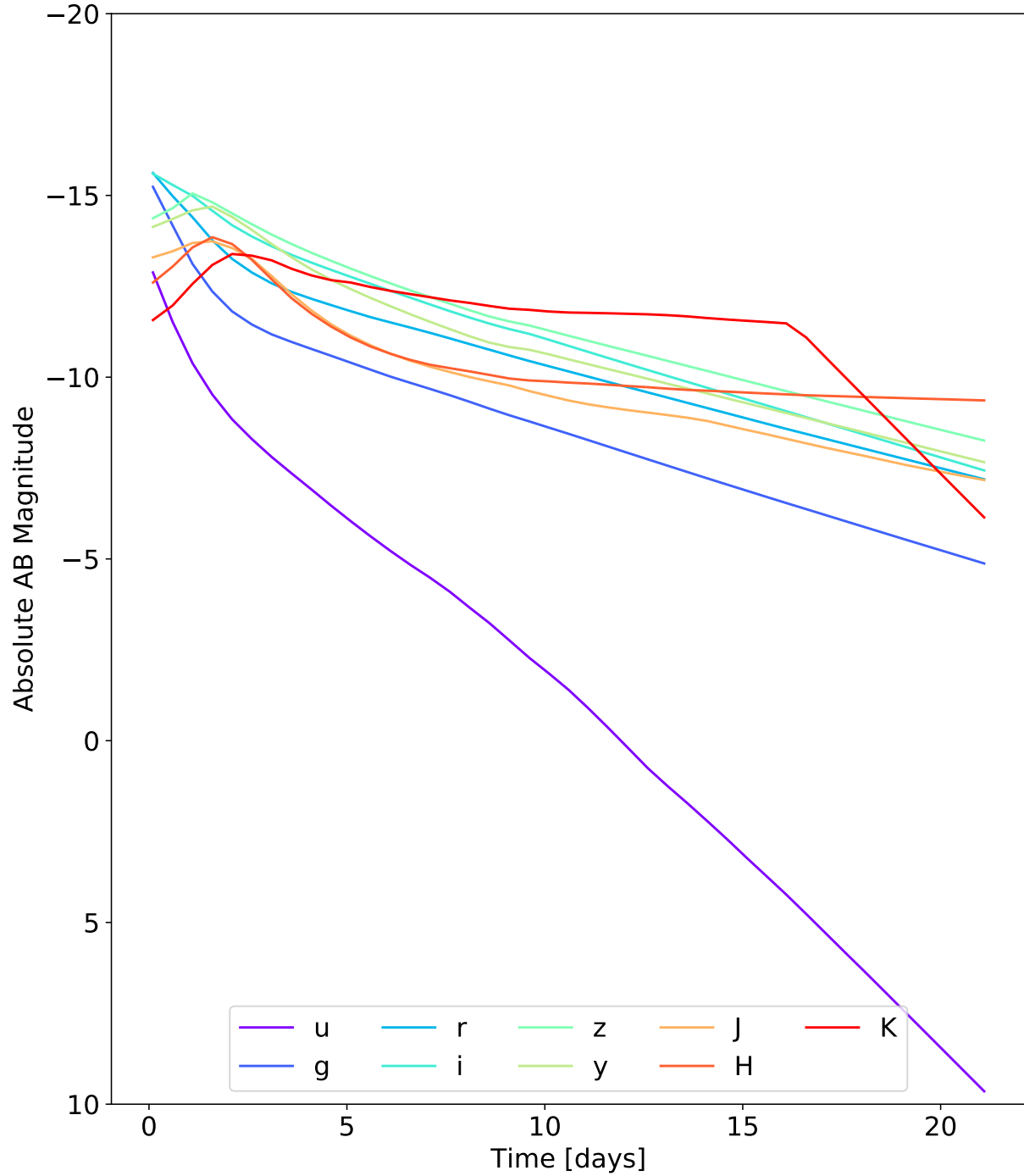


Figure 17: AB magnitude in different passbands, computed with our KN model using gwemlightcurves. We use $m_1 = 1.5858M_{\odot}$, $m_2 = 1.1989M_{\odot}$, and $\chi_{\text{eff}} = 0.029$.

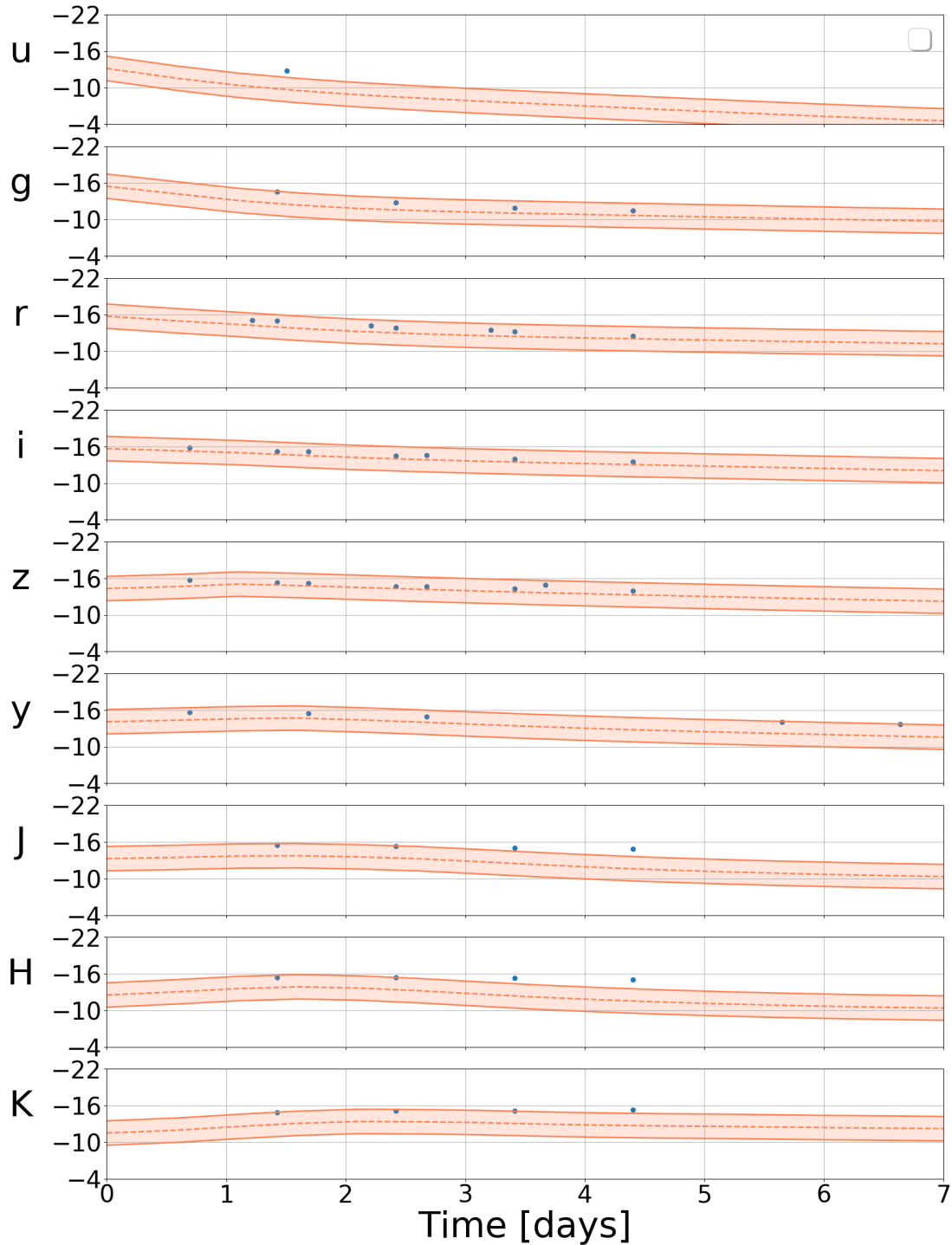


Figure 18: Predicted AT2017gfo lightcurves from our model (orange), compared to observations taken from [60] (blue). It should be noted that these observations have errors of maximally ~ 0.2 mag, so these are not visible in this graph. The dotted line represents the median (50th percentile) of the lightcurve distribution from the input values depicted in Table 2. We also plot a realistic error budget of 2 mag. We use the AB magnitude system.

the input values are based on the median values of the GW parameters m_{chirp} , q , and χ_{eff} . The error on these quantities is quite large, which means that the uncertainty on the input parameters and in extent to that on the lightcurve is also substantial. As a result of this, the lightcurve may have errors of ~ 2 mag. We plot this uncertainty in Fig 18. We can see that the model recovers the observations well within the specified error budget; particularly the r , i and z bands are accurately depicted by this model. Only few observations fall outside the predicted range.

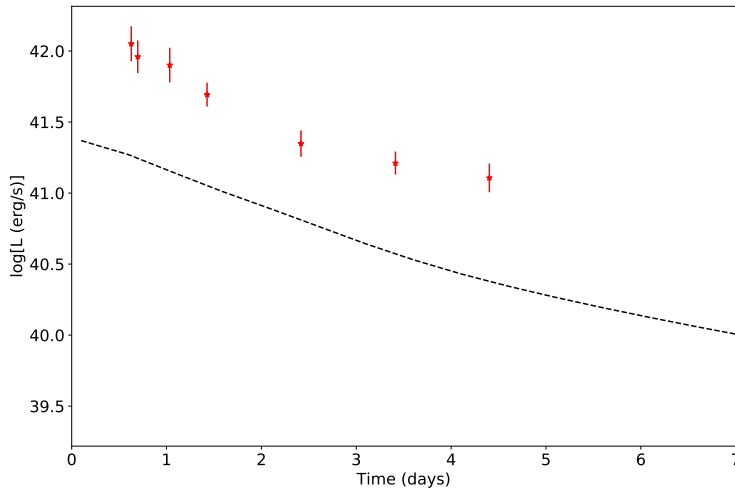


Figure 19: Bolometric luminosity resulting from the KN model with input values $m_1 = 1.5858M_{\odot}$, $m_2 = 1.1989M_{\odot}$, and $\chi_{\text{eff}} = 0.029$. Observations are taken from [60].

We also depict in Fig. 19 the bolometric luminosity of the KN, as a function of time. We compare this with observations from [60]. The general shape of L_{bol} is recovered quite well by our model; we see a steady exponential decay that is present both in our predictions and in the observations. However, we clearly underestimate the luminosity by about half an order of magnitude. Still, with the large uncertainty that arises in the magnitude computation due to the uncertainty in input values, the curve for the median luminosity shown here may contain significant errors as well. After all, the bolometric luminosity is computed from the magnitude in all bands. A difference of 2 mag in a lightcurve can lead to a bolometric luminosity that is ~ 1 order of magnitude higher or lower. Therefore, also in this regard, we may conclude that the bolometric luminosity is predicted reasonably well within the expected error range.

It is important to note that the input values we use (specifically m_1 , m_2 , and χ_{eff}) are supposed to be the most likely ones for GW170817, according to [61]. Still, with these values, we can see from Figs. 18 and 19 that we generally underestimate the brightness of AT2017gfo. This suggests that the KN model has some built-in inaccuracies. We have seen that the values we find for m_{ej} and v_{ej} are in fact typical, so we are tempted to say

that there could be some discrepancy between the input ($m_1, m_2, \chi_{\text{eff}}$) and the values for m_{ej} and v_{ej} that eventually causes the dim lightcurves. In other words, where our m_{ej} and v_{ej} may be typical, it is well possible that they do not correspond with the specific model input values we use. After all, we compute the total ejecta mass and velocity from fits with the NS properties, rather than analytical or physical relations. Once again, to see how the fitting formulae model the relationship between the NS masses and m_{ej} & v_{ej} , we refer the reader to [61]. Generally, in order to make our predicted lightcurve fit with observations, we would have to increase the ejecta mass and/or velocity. A higher ejecta mass leads to a brighter and longer KN lightcurve, and a higher ejecta velocity makes the KN brighter, but shorter as the ejecta expand faster [61]. We find that using $m_{\text{ej}} \approx 0.04M_{\odot}$ and $v_{\text{ej}} \approx 0.2c$ results in a much better fit with the AT2017gfo observations in [60]. With this, we highlight the limitations of the fitting formulae. However, given the fact that many uncertainties exist in the link between BNS component masses and the eventual ejecta mass and velocity, fits are currently the only way with which we can approximate the NS mass - ejecta mass relationship. Therefore, of course, using fitting formulae is not problematic, but we should still keep in mind that this could lead to inaccuracies in our lightcurves. Still, if more accurate fitting curves are developed (e.g. [48] for the disk mass), they could be implemented in the KN model. The same goes for the NS EOS: if in future, more constraints are placed on the NS interior and certain EOSs appear favourable, these can be used in this model instead.

We also list several other limitations, which when taken care of, may make this model more realistic. First, including an inclination angle may be an aspect that one could add. Where KN emission is generally isotropic, there may still be fluctuations in the spectrum as well as the overall brightness, as a result of the inclination angle. For example, for edge-on viewing angles (i.e. 90° with respect to the binary rotation axis), the high opacity of the lanthanide-rich matter in the disk may block the "blue" emission [22]. Additionally, the assumptions for X_{lan} may have some room for improvement as well [61]. Where we fixed this quantity to a single value, this may in reality be a more complicated distribution. Please note that these two suggestions for improvement are ones that would (probably) not significantly impact the computation time of this model. Of course, since this is a 1-dimensional model, upgrading to more dimensions such as *Model II*-like⁶ frameworks ([19, 15]) could improve the performance even more. However, this would significantly increase the computation time, which is highly undesirable for the Toolbox.

To wrap up this Section, we can say that this KN model recovers the general shape of the lightcurves in different passbands as well as the bolometric luminosity quite well. At the same time, it clearly underestimates the brightness of AT2017gfo, which is likely to be a result of built-in oversimplifications. Though, for the Toolbox and all its purposes, we can conclude that this model is acceptable: its computation does not take long, and its predictions correspond with observations within an expected (large) error range.

⁶We deliberately say "*Model II*-like", because *Model II* itself has proven to be less accurate than *Model I* in [61].

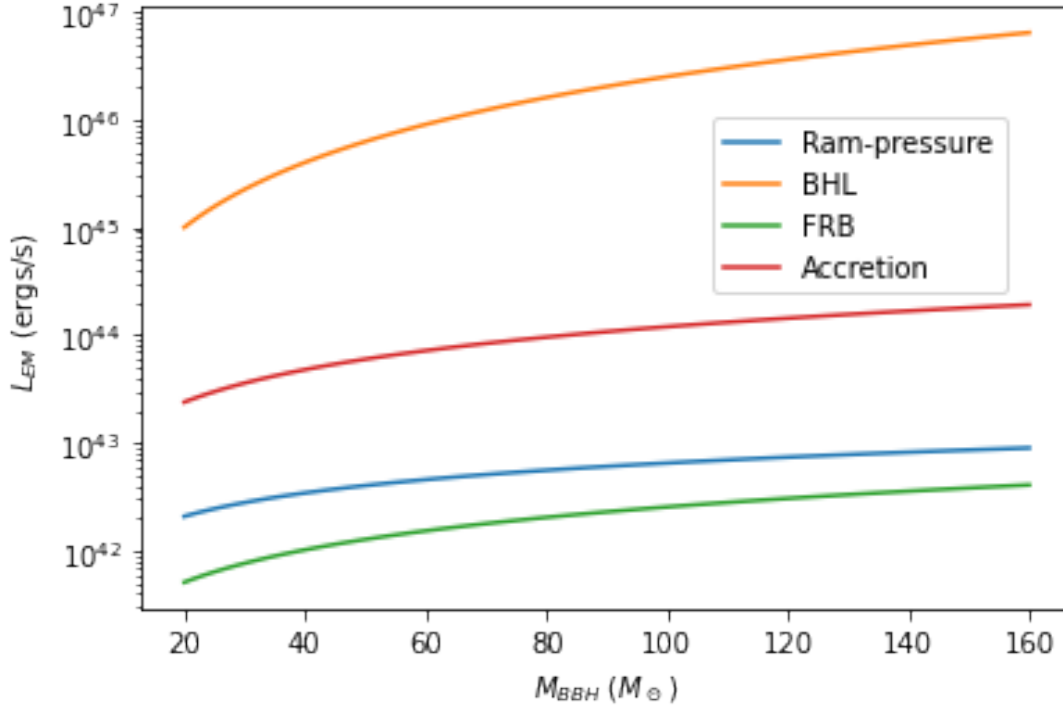


Figure 20: Stellar mass BBH luminosity as a function of BBH mass, predicted by each of our four different models.

3.3 Stellar mass binary black holes

Here, we briefly report the estimated luminosity from our four different models. In Fig. 20, we show the EM luminosity as a function of total BBH mass, for each model with the fiducial parameters that we list in Section 2.2. We observe that all of them have a similar shape; an initial steep rise (NB: the y-axis is a logarithmic scale) for low masses, which eventually flattens as one goes to higher BBH masses. The plots show no overlap, but rather seem to be approximately shifted vertically with respect to one another. Clearly, with the fiducial parameters we employ, the BHL model is the one that generates the highest luminosity, regardless of the mass. Also, this is the model that shows the largest difference in luminosity between the lowest and highest BBH mass. The ram-pressure stripping model and the FRB appear most similar. Still, overall, these models cover a luminosity range of $\sim 10^4$ ergs s^{-1} . This highlights the uncertainty that exists in the EM signatures of such setups. Still, it is good to see that this range is not extremely wide, so at least these models agree with one another within several orders of magnitude. Therefore, whilst also keeping in mind their lower priority, we deem these models good enough for a first version in the Toolbox.

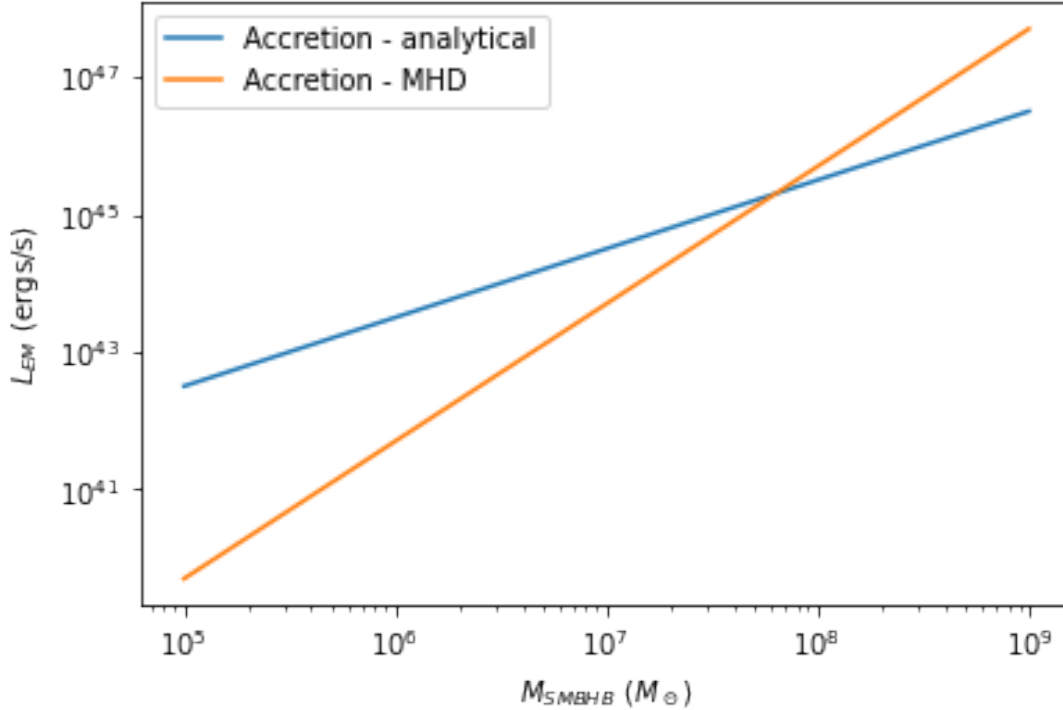


Figure 21: SMBHB mass vs. accretion luminosity, for both our luminosity-estimating models.

3.4 Supermassive black hole binaries

For completeness, in this Section, we show the results of our SMBHB luminosity estimates in a similar fashion as the stellar BBH case. In Fig. 21, we show the SMBHB accretion luminosity as a function of total SMBHB mass, corresponding to the two models we explain in Section 2.3. We see that the analytical model predicts higher luminosities for lower masses, where a turning point happens at $\sim 10^8 M_\odot$, beyond which the model derived from MHD simulations gives higher luminosities. Where their shapes are slightly different, both models remain within two orders of magnitude for typical SMBHB values. As such, also here, we can conclude that these predictions are good enough for a first version in the Toolbox. As we move closer to SMBHB GW detections, at some point more accurate models will be developed, which could eventually be integrated into the Toolbox framework.

3.5 Toolbox and EM counterparts

It is of the utmost importance that we bridge the gap between our theoretical frameworks and functioning EM models that are integrated into the Toolbox. In this section, we put this into practice by illustrating the trade-offs by GW and GRB detections. We use the Toolbox to simulate a universe filled with BNSs that are to be detected by a

specified GW detector. For each detected event, we save the binary characteristics (e.g., $m_1, m_2, \chi_{\text{eff}}$). To make the connection with GRB signatures, we also save for each event the viewing angle i with respect to the binary orbital angular momentum (and thus the jet axis, i.e. $i = \theta_v$), as well as the distance D . From there, using our GRB model, we calculate the peak GRB flux for every event. As such, this allows us to make plots of the detected flux against binary characteristics, as well as discuss the detectability of EM counterparts by different EM instruments. This way, we can illustrate the large amount of additional functionalities that the Toolbox will gain after we will have integrated models for EM signatures.

We run the Toolbox for two different configurations: for the first one, we run advanced LIGO (design sensitivity) for 10 years. Additionally, we investigate BNS events from the ET, which we run for 1 year. For computational cost related reasons, we have to decrease the size of the ET dataset by a factor 4. In both cases, we use the standard SNR threshold of 8, as well as the flat Λ CDM-Planck18 cosmological model [18]. To be able to compute the peak flux for every event, we need to input several parameters. From the binary characteristics we can take from the Toolbox, we use the distance D and inclination angle i (i.e. θ_v) for each event. For the free parameters γ, r_0 , and ν'_0 , we use the same typical values as for our comparison with GRB170817A: $\gamma = 275, r_0 = 10^{13}$ cm, and $\nu'_0 = 1 \times 10^{19}$ Hz. We utilise the distribution reported in [23] for our estimate of $\Delta\theta$: a normal distribution centered around 16° , with $\sigma = 10^\circ$. We manually add in a floor value of 1° , as this is around the maximum $\Delta\theta$ for which our numerical integration in Eq. 13 does not encounter resolution issues. For each event, we draw a random number from this distribution to obtain $\Delta\theta$. To generate the total GRB energy E_{GRB} , we adopt the results from [24], which reports that the range of E_{GRB} can be approximated by a Gaussian distribution around 5×10^{50} ergs, with a 1σ multiplicative factor of 2. We take a random number from a normal distribution with these characteristics. With these parameters, we compute the peak flux of each GRB within the specified detector frequency sensitivity window ($[\nu_1, \nu_2]$) by integrating νF_ν between ν_1 and ν_2 , and then returning the highest flux between T_{start} and T_{end} . In doing so, we will use two different GRB instruments (Fermi/GBM and Swift/BAT) to highlight the influence of the detector sensitivity.

In the following, we will first investigate some general trends that we observe in the GW detections which are relevant for EM observations as well. After that, we will illustrate the working of our GRB model by showing how the GRB flux and detectability is influenced by different binary parameters. We will also comment on where GW170817 lies within the observed populations.

3.5.1 GWs

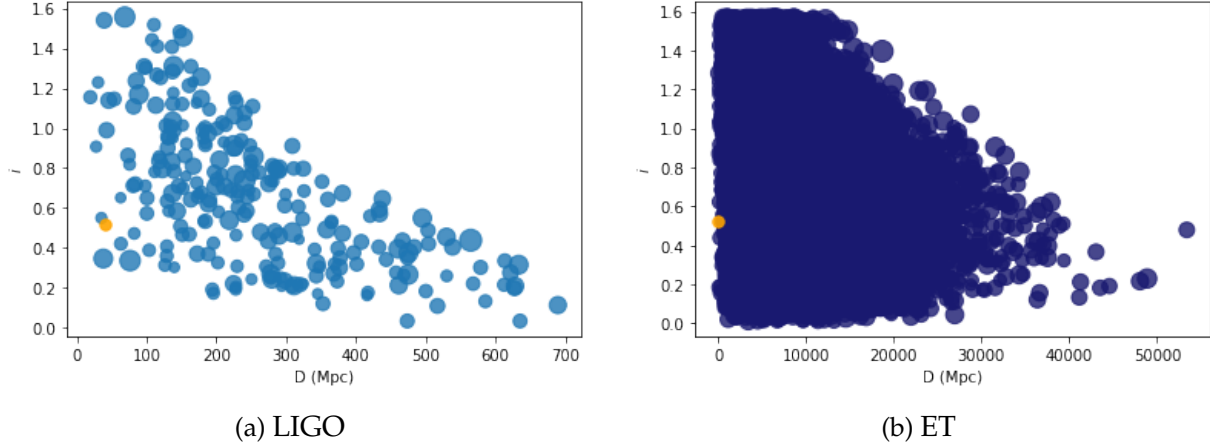


Figure 22: Inclination angle i (i.e. θ_v) as a function of distance D (Mpc). The larger the circle, the larger the binary mass. We plot GW170817 in orange.

We start this Section by discussing some of the GW characteristics that we can infer from the Toolbox simulations. It should be noted that there are many properties to discuss, but the most relevant quantities to the flux of sGRBs (i.e. the ones we will show) are the inclination angle and the luminosity distance. We will explain the relevant physics of the GW detections from the plots in Fig. 22. Here, we depict the binary inclination as a function of distance, for all BNSs that are detected in the Toolbox. We show this for LIGO (left), and ET (right). GW170817 is plotted in orange, to illustrate where this detection can be placed. In these plots, we can clearly see a pattern. If one were to draw a diagonal from the top left to the bottom right, almost all events would be on the left of this diagonal. Here, we are in the presence of a GW detection bias; clearly, events with both a high inclination and large distance are not detected by both LIGO and the ET. (compare with ET) The explanation is twofold: first of all, this is due to the fact that binaries that are viewed at larger angles (i.e. towards edge-on) show significantly less strong GW signals. Additionally, the GW strain is lower for larger distances [50, 59, 62]. In these plots, we also show the total binary mass by varying the dot size. Concerning the mass, we see no trends in Fig. 22a. We observe that GW170817 has quite a low inclination angle and distance, as compared to other detections by LIGO, and especially the ET. It should be noted that the advanced LIGO design that we use here is significantly more sensitive than the advanced LIGO that detected GW170817. Then, of course, this LIGO design is able to observe BNSs further away and at higher inclinations than GW170817. Still, it should be noted that GW170817 is the closest GW source detected by LIGO, so even in a similar plot for the 2017 LIGO sensitivity, it would be on the (far) left [4]. Fig. 22b really highlights the significantly higher sensitivity of the ET; the shape of the plot is similar, a lot more sources are detected. Where this LIGO design finds 238 BNSs in 10 years, the ET observes more than 168,000 (where we depict $\sim 42,000$ here) in

1 year. Additionally, ET detections stretch out to much larger distances, corresponding to lower GW strain on earth. Interestingly, for ET, at the highest distances very few to no GW detections are done; this instrument makes only a handful observations beyond $\sim 30\text{-}40$ Gpc. This is due to the fact that there simply are much less GW sources at such distances, as we run out of universe. To illustrate, a GW source at a distance of 35 Gpc corresponds to a cosmological redshift of ~ 3.9 . Moreover, at these distances, we see that most GW detections are centered around $i \approx 0.8$ ($\sim 45^\circ$). This preferred inclination angle is a combination of i) the fact that the GW strain is stronger for lower inclination angles, and ii) the area of the celestial sphere (at some fixed D) gets larger for increasing i , according to $\sin(i)$. Because there are so few detections beyond 30-40 Gpc, at such distances this preferred inclination angle becomes apparent.

3.5.2 Joint GW-EM detections

With some knowledge on the GW detections of these datasets under our belt, we can move on to illustrating joint GW-EM detections. In Fig. 24, we depict the peak GRB flux as a function of inclination angle, respectively for LIGO-Fermi/GBM, LIGO-Swift/BAT, and ET-Fermi/GBM. Let us first compare the number of EM detections for these three different cases. All points above the red horizontal line in each plot represent detected GRB by the corresponding GRB instrument. We report respectively 88 (detection fraction of 0.37), 86 (fraction of 0.36), and 5389 detections (fraction of ~ 0.13). A first thing that stands out is the fact that Swift/BAT shows an almost equal number detections as Fermi/GBM, despite its much narrower frequency range. The sensitivity band is 15-150 keV for BAT, whereas it is 10-40000 keV for GBM⁷. This similarity in GRB detections is the result of the fact that GRB spectra typically peak within a few 10 to a few 100 keV. A place where we *do* see the impact of the narrower Swift/BAT frequency band is in the values for the peak flux; Fig. 24a generally shows a higher peak fluxes than Fig. 24b, because Fermi/GBM can detect a larger part of the GRB spectrum.

Regarding Fig. 23, we see a similar pattern in each graph; clearly, there is a tail of detections in which the peak flux decreases significantly as a function of increasing inclination angle. We have to stress that, technically, the peak flux is mainly influenced by the *difference* between θ_v and $\Delta\theta$, rather than θ_v (i.e. i) alone. Whether a GRB is viewed on-axis or not, and if not, how far off-axis makes a large impact on the peak flux (see also Fig. 11). Still, as $\Delta\theta$ does not vary as much in our model as θ_v , showing θ_v vs F_{peak} still shows the same characteristics as $\theta_v - \Delta\theta$ vs. F_{peak} . The tails in Figs. 24a and 24b correspond to off-axis cases. For the off-axis scenario, the more the observer is tilted away from the jet beam, the less flux they will observe. Another thing we notice in Figs. 23a and 23b is the fact that there appears to be some sort of gap between a cluster of high fluxes and the tail of the main group of events. We can attribute this to the large difference in flux between the off- and on-axis case. As we established,

⁷See https://fermi.gsfc.nasa.gov/ssc/data/analysis/documentation/Cicerone/Cicerone_Introduction/GBM_overview.html and https://swift.gsfc.nasa.gov/proposals/tech_appd/swifftta_v14/node26.html

3 Results and discussion

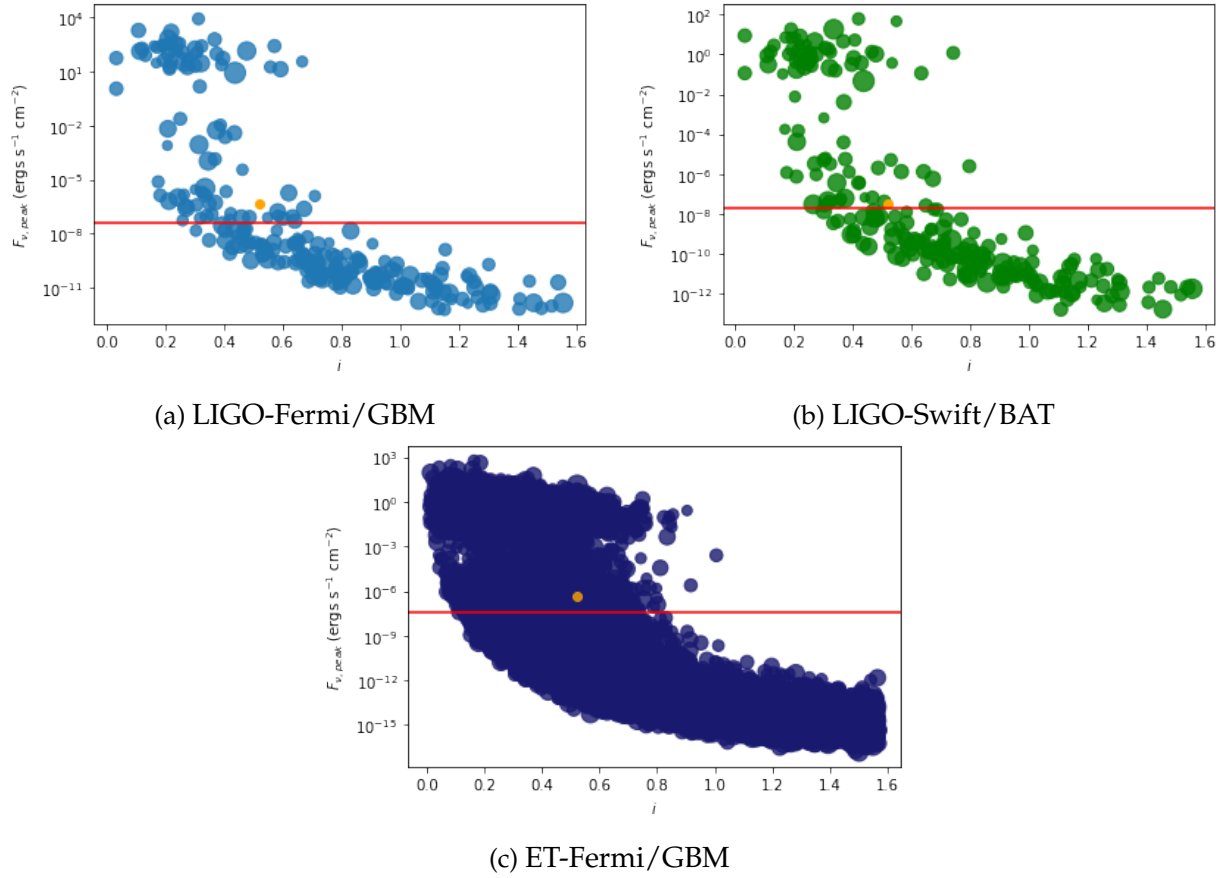


Figure 23: Peak flux within in the specified detector frequency range, as a function of inclination angle. Also, here, we plot GW170817 in orange and the dot size represents the binary mass. The horizontal lines represent the flux threshold for each corresponding GRB instrument.

due to the beaming effect, in the on-axis case, the viewer will observe very high fluxes concentrated in a narrow peak. Where the tail mostly represents the off-axis cases ($i > \Delta\theta$), the clusters at the top correspond to on-axis scenarios, where $i < \Delta\theta$, whose peak flux is significantly higher. Though, we still see *some* BNSs inside the gap that arises as a result of the difference between on- and off-axis scenarios. These GW events are those that are either on-axis with disfavourable properties, or off-axis with favourable properties. For example, an on-axis GRB that is very far away will likely have a peak flux that falls within this gap. With enough detections, this gap disappears, as we see in Fig. 23c. A next aspect that stands out is the fact that Fig. 23c shows that the highest possible flux decreases as the inclination angle increases, starting at $i \approx 0.25$; we observe a decreasing plateau at the top of this graph. The explanation of this is as follows: the maximum peak flux happens when the centre of the jet is right in the line-of-sight of the observer, i.e. at $i = 0$, or close to that. When the inclination angle is close to the jet edge (i.e. $\Delta\theta$), the ring of points (see Fig. 12, middle panel) at the instant T on which the peak flux happens, lies partially *outside* the jet, so a slightly lower flux will be detected.

3 Results and discussion

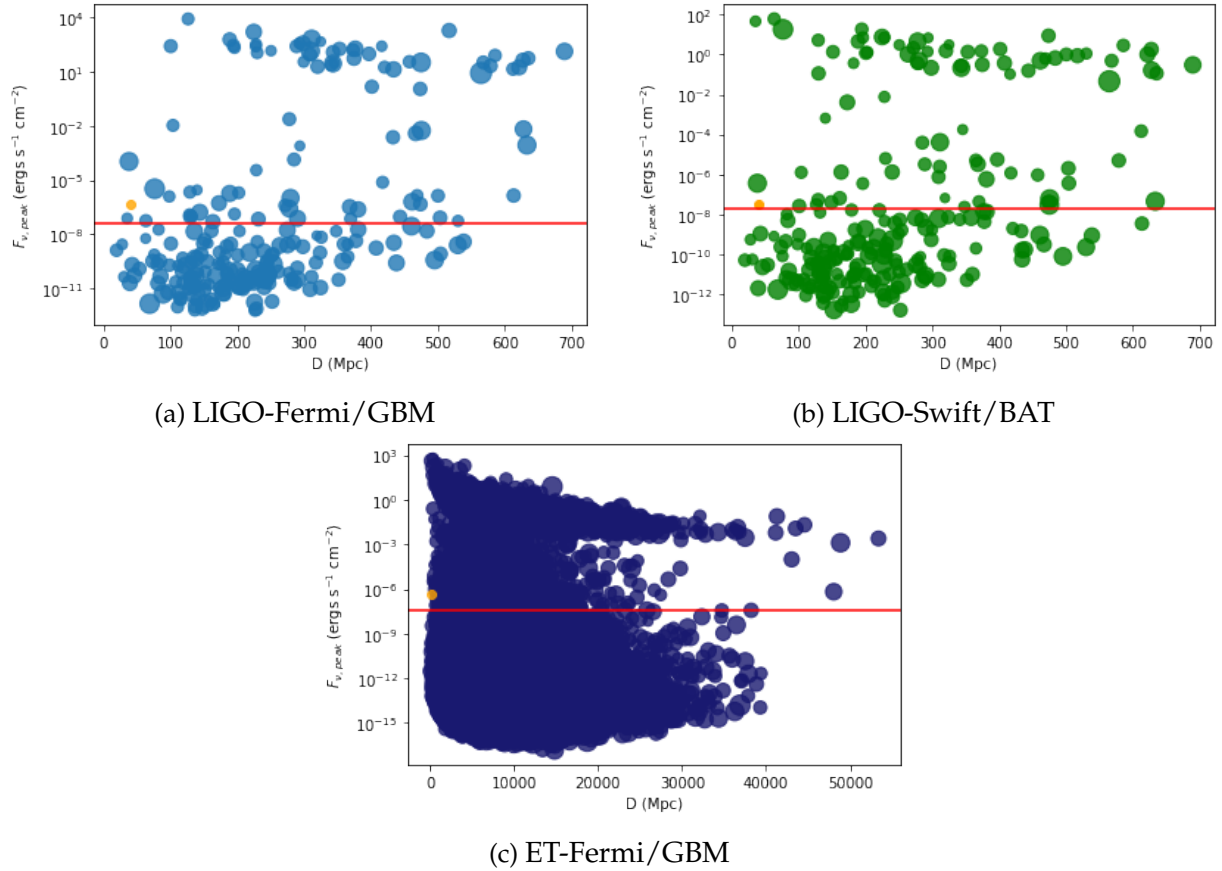


Figure 24: Peak flux within in the specified detector frequency range, as a function of distance. Also, here, we plot GW170817 in orange and the dot size represents the binary mass.

This becomes apparent when i is just slightly less than $\Delta\theta$. In our case, $\Delta\theta$ is typically 16° , which is equal to ~ 0.28 rad. Therefore, it is only logical that we start to see this effect from 0.25 rad onwards. From here, the higher the inclination angle, the lower the maximum peak flux. We observe that the highest on-axis inclination angles lie at about 0.9, with fluxes of $\sim 10^0$ for ET-Fermi/GBM. Lastly, we would like to note that the GW170817 properties in this regard are quite average and typical.

We can explore more characteristics of the joint GW-EM detections by investigating how the peak flux behaves as a function of distance. We show this in Fig. 24. Firstly, in the top panels, we appear to see a cluster of GW detections at low distances with low peak flux. Where this looks strange, it is in fact quite logical when one looks at Fig. 22a. Here, we see that LIGO simply detects a large amount of sources with $D = 100 - 300$ Mpc and $i = 0.5 - 1.2$. Even though these systems are close, which is favourable for a GRB detection, their inclination angles are quite high; they are typically observed quite far off-axis, i.e. ~ 13 to 53° . Given the large influence of the inclination angle on the observed flux as we have seen, it is not surprising that these events are not detected electromagnetically. Clearly, also here, we observe a gap between low and high fluxes,

3 Results and discussion

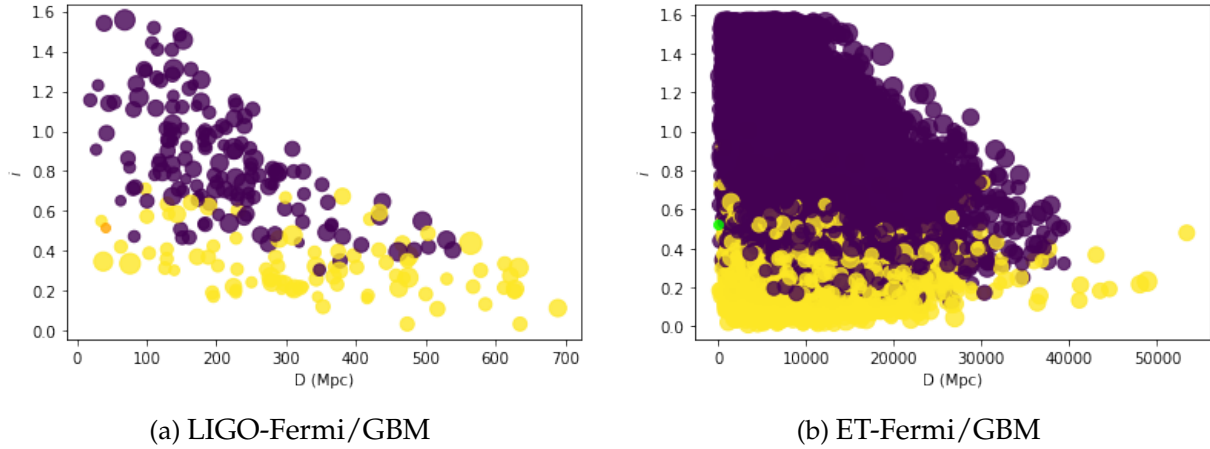


Figure 25: Inclination angle as a function of distance, for LIGO (left) and ET (right). EM detections by Fermi/GBM are depicted in yellow. We show GW170817 in orange (left) and lime (right).

which we can attribute to respectively off- and on-axis scenarios. We compare the gap for LIGO-Fermi/GBM (top left panel) with the gap for ET-Fermi/GBM (bottom panel). Clearly the ET shows a less significant gap. Since it generally detects more systems, it also detects more systems with intermediate flux that fill the gap. Still, for ET, we observe some empty space in places where it detects less sources, i.e. above ~ 28 Gpc. Also here, the on-axis mergers are clearly separated from the off-axis ones. When comparing the fluxes of the gap with those in Fig. 24a, we see that it covers *lower* fluxes than the gap in Fig. 24a. The reason for this is the fact that the BNSs that LIGO observes are generally much closer than those detected by ET. Since the GRB flux is a function of $1/D^2$, it is indeed expected that we see a gap at lower fluxes for ET. The impact of the distance on the GRB flux is nicely visible especially in Fig. 24c. With increasing distance, we see that the maximum peak flux slowly declines. Lastly, also here we can make some comments on GW170817. Next to the fact that it is very close, it is also quite bright for an off-axis GRB. Where the majority of off-axis bursts is not detected for LIGO BNSs (top two panels of Fig. 24), this one is right above the flux threshold for both Fermi/GBM and Swift/BAT.

For more insight into the influence of i and D on the GRB detectability, we include Fig. 25. Here, we show the same as in Fig. 22, but this time we depict in yellow those GW events that are also observed electromagnetically. Clearly, we can see that the distance plays only a small role in the detectability of the GRB as compared to the inclination angle. Even at the lowest distances, if the inclination angle is not below ~ 0.8 , the GRB is not detected. Both for LIGO and ET, at the highest distances, which correspond to lower inclination angles due to the GW selection bias, almost all GW events have observable GRB signals. This once again highlights the crucial role of the orientation of the observer with respect to the relativistic jet.

4 Towards implementation

Even though this project is mainly concerned with the modelling of EM counterparts of GW sources rather than implementation into the Toolbox framework, it is still vital that we provide an outline for the implementation. We will do so in this section, by illustrating what the Toolbox will look like with our addition, as well as the steps to achieve this. By realising a sensible implementation, it is especially important to keep in mind the general purpose of including EM models as well as of the Toolbox itself. The updated Toolbox should be set up such, that investigation of the trade-offs between GW and EM observations in a somewhat detailed fashion is possible. Moreover, the in- and output should not be so detailed that the computation time severely suffers from this. Of course, an optimal way to achieve this does not exist, as this is highly subjective. In this section, we propose a way of implementation that we deem suitable. It should be noted that this may still be subject to change. For example, if users wish to use the Toolbox for GW-EM synergies in ways that is not possible with the proposed implementation, we should adapt the Toolbox usability to their general needs. In the following, we will set out our intended implementation for two categories: first, we explain how the GRB and KN after BNS/BH-NS will be integrated. After that, we will generally discuss how the luminosity of stellar & supermassive BBHs will become part of the Toolbox.

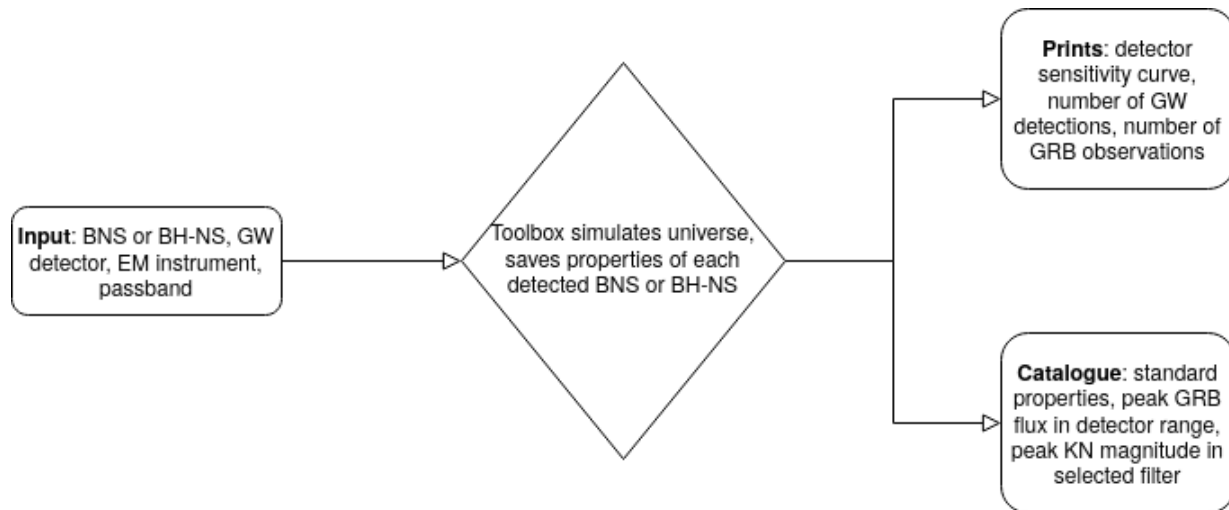


Figure 26: Flowchart of the BNS/BH-NS option, with implemented models for GRBs and KNe.

In Fig. 26, we depict a flowchart of how the Toolbox is to be used when we will have included models for sGRBs and KNe. A general idea of the user interface is shown in Fig. 27. This setup is the case for both BNS and BH-NS. Next to the standard input parameters, we allow the user to select an EM instrument for GRB observations (e.g. Fermi/GBM or Swift/BAT), as well as a photometric filter (g , r , i , z , y , J , K or H) in which we would like to investigate KN emission. When simulating the universe with

4 Towards implementation

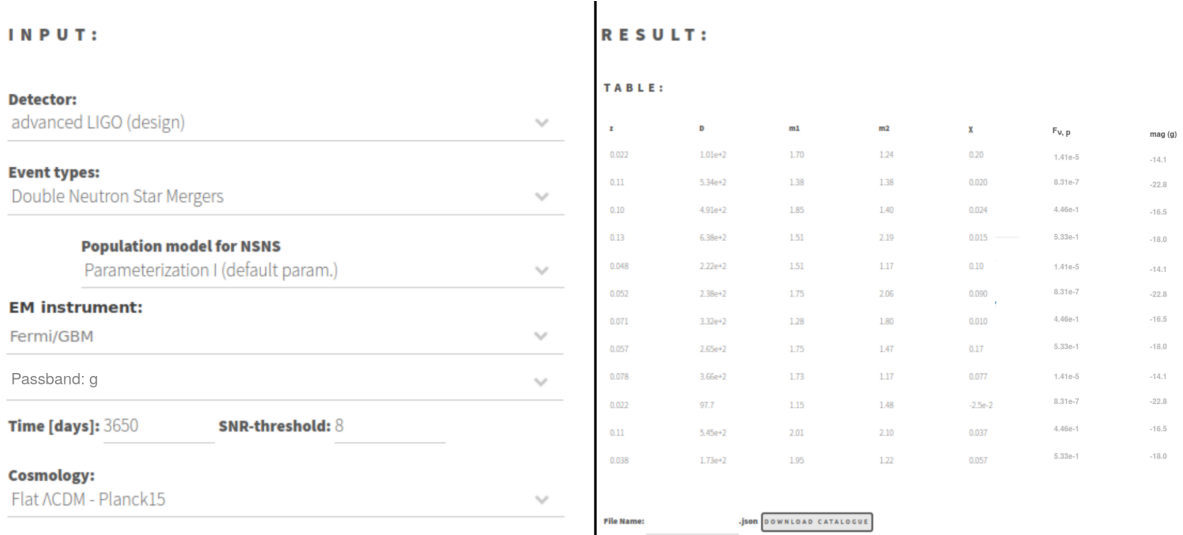


Figure 27: Illustration of the user interface of the Toolbox, where we have implemented the EM models for BNS and BH-NS. We show the input boxes, as well as the resulting catalogue.

BNSs or BH-NSs (depending on which of these two was selected), for each event, the Toolbox computes the peak F_{ν} of the GRB within the sensitivity range of the selected GRB detector. Additionally, for each GW event, we compute the KN lightcurve within the passband that was selected by the user. Subsequently, the Toolbox returns a plot of GW sensitivity curve, as well as the expected number of GW detections and EM observations. Additionally, the GRB peak flux and peak magnitude in the KN lightcurve are saved in the catalogue that serves as the main output.

Clearly, in this setup, the GRB operates as the "main" EM counterpart. We justify this choice by drawing parallels with the EM observational procedure after GW170817. Here, the GRB was the first detected EM output resulting from the BNS in GW170817. Exactly this observation triggered the launch of an extensive observing campaign to look for more counterparts of this event. Without the GRB, the KN and afterglow may have never been detected at all, or associated with GW170817. Despite the central position of the GRBs in the Toolbox, we still deliberately do not compute or save the complete spectrum of each GW event. Where this would allow for quite detailed investigations, it would not be feasible with regards to the computation time. Saving the peak flux of each event in the catalogue is a good compromise between these two conditions. Additionally, the significance of the GRB has lead us to include the extra drop-down menu where one chooses a GRB detector. We could have simply saved the peak flux and corresponding ν in the catalogue without the need for specification of an instrument, but for an EM counterpart as significant as this, we deem it important that the Toolbox can immediately make predictions related to the EM detectability. Moreover, as we mentioned in Section 3, the peak GRB flux within a detector sensitivity range does not necessarily correspond to the *actual* peak flux. By immediately providing the GRB detector along with its range and detection threshold, we prevent any inaccuracies that

4 Towards implementation

TABLE :

z	D	m1	m2	x	L
0.31	1.65e+3	46.4	40.4	-9e-3	1.5e42
1.1	7.46e+3	52.9	37.3	0.22	0
0.28	1.49e+3	36.8	21.5	-7.1e-3	0
0.62	3.79e+3	44.0	24.7	0.016	0
0.76	4.84e+3	34.8	29.3	-1.1e-3	3.3e41
0.40	2.24e+3	9.14	7.05	-1.9e-2	0
0.19	9.82e+2	39.1	19.2	-2.5e-2	0
0.86	5.64e+3	19.2	10.4	0.063	5.7e42
0.73	4.61e+3	39.6	36.7	-3.7e-2	0
0.36	2e+3	8.91	7.49	0.014	0
0.38	2.13e+3	21.7	15.4	0.060	0
0.39	2.15e+3	33.5	28.1	-1.3e-3	0

File Name: .json [DOWNLOAD CATALOGUE](#)

Figure 28: Illustration of the catalogue, for the stellar BBH mergers after implementation of our EM models.

could arise from this discrepancy. In the context of the GRB being the main EM counterpart, the implementation of the KN model will be slightly simpler. To be able to study characteristics and patterns of joint GW-KN observations, returning a peak magnitude in a specified photometric band is believed to be sufficient. The user with interests in this regard can download the catalogue in which this information is saved, and compare with magnitude detection threshold of KN-observing instruments. Once again, to save computational cost, we limit the output by simply supplying the peak magnitude in a single passband, rather than an entire lightcurve for all filters.

A possible future addition to the Toolbox will be the possibility to investigate the characteristics of a single GW source. One could insert a set of source parameters, after which the Toolbox would return more detailed GW-related properties. For this option, we could use our EM models to supply more information than just peak fluxes and magnitudes. Here, for a single BNS or BH-NS, we could provide the entire spectrum at different moments in time during the GRB pulse, along with the complete lightcurve in all photometric passbands.

The procedure for the EM counterparts of stellar and supermassive black hole binaries will be slightly simpler, as we only give an estimate of their luminosity. An illustration of what the Toolbox will look like when EM signatures of these mergers have been implemented is depicted in Fig. 28, for stellar-mass BBHs. Here, one can see that

the user can select one of the models we explained in Section 2. When we run the Toolbox, the EM luminosity is computed using the selected model, and added as an extra column to the catalogue. Note that not all BBHs in the catalogue will get a non-zero luminosity. After all, only a fraction of BBHs resides within AGN disks and will show EM signatures. To account for this, we use the rate of BBH mergers in AGN disks along with the total rate of BBH mergers to find the fraction f_{EM} of BBH mergers that will have EM output. For each detected BBH, the Toolbox will draw a random number from a uniform distribution between 0 and 1. If that number is lower than or equal to f_{EM} , that BBH will get a luminosity according to the selected model. If it is higher, we will assign a luminosity of 0 ergs s^{-1} .

5 Summary & conclusion

In this Section, we will summarise all of our findings, as well as provide insight on future plans to include our models into the Toolbox with the proposed implementation. In this thesis, we have argued why the GW Toolbox is a program that can be of great assistance both for scientists within and outside the GW community. The Toolbox allows for quick and efficient investigation of GW source characteristics and detectabilities, as well as detector capabilities. The user-friendly fashion in which the Toolbox operates also allows non-experts to get quick yet useful insight into GW detectability related concepts, something that is especially important in the current era of physics, in which GWs are at the forefront. Next to this, we have argued why adding models of EM counterparts to GW sources would significantly increase the usability of the Toolbox. As we are currently living in the era of multi-messenger astronomy, many joint GW-EM detections will be made in the near future. This also means that more and more astronomers and GW astrophysicists will do research in which their respective fields overlap. In this brand new era, a tool with which one can study the synergies and trade-offs between GW detections and EM observations certainly has the potential to be extremely useful to provide anyone within GW-related research with more knowledge and a better understanding of GW sources.

In this project, we have taken on the task of creating models of EM counterparts to GW sources, in order to eventually add them to the GW Toolbox. We have chosen to set up models for EM signatures to BNS and BH-NS (sGRBs and KNe), stellar BBHs and supermassive BBHs. Our most extensive model is the one for the sGRBs, followed by the KN model. We have, first, investigated the conditions for the occurrence of GRBs and KNe after BNSs and BH-NS. After this, we have explained the general framework of our models. For the sGRBs, we use as a base an analytical top-hat jet structure GRB model by [34], which allows for computation of the time-evolution of the GRB spectrum. We have collected information from various sources in order to recover typical GRB light-curves as accurately as possible. For our KN model, we use a framework described in [61], where one can use the program `gwemlightcurves` to simulate KN lightcurves, based on binary parameters (NS masses, effective spin and EOS). This model computes the KN ejecta mass and velocity from fitting formulae, after which it can generate light-curves using information from radiative transfer simulations. For stellar BBHs and SMBHBs, we have collected models that can give order-of-magnitude luminosity estimates. As EM counterparts of these two types of GW sources have not been observed yet and many different predictions exist, we decided not to make these frameworks too extensive.

We have illustrated the general working of our GRB model, by varying its input parameters (most importantly the viewing angle θ_v), and infer GRB characteristics from this. We have provided a visual breakdown of each aspect of the predicted GRB spectrum. With this model, we have tried to emulate the observables of GRB170817A. We have employed values for the input parameters, that collectively resulted in a good agreement with the GRB170817A characteristics. For each input value, we have argued

whether it was typical for GRBs. We have established that only the total GRB energy was slightly atypical, but ascribed this to the fact that GRB170817A may have been atypical itself, in the sense that it was intrinsically faint. Our final verdict on this model was that it was good enough to be used in the Toolbox. For the KN model, we have followed [61] and inserted expected values for the NS masses and spin of GW170817 into `gwemlightcurves`, in order to generate KN lightcurves. By analysing the shape and relative brightnesses of the lightcurves in different passbands, we have established that this model is able to recover the typical KN spectrum quite well. By comparing the lightcurves and bolometric luminosity with observed values of AT2017gfo, we have found that this model slightly underestimates the brightness of the KN counterpart to GW170817. Still, the results lie within expected (relatively large) error bounds, so we deem it acceptable. Moreover, we have illustrated the working of EM models in the Toolbox by computing the peak GRB flux for a set of simulated BNS events with the Toolbox, for different GW detectors (LIGO and ET), as well as different GRB instruments (Fermi/GBM and Swift/BAT). We have investigated the trade-offs between these two kinds of detectors, and looked at the importance of certain binary properties on joint observations. We found that the inclination angle i (i.e. θ_v) has the largest impact on the GRB fluxes and detectabilities.

Lastly, we have provided a plan for how our models will be implemented into the GW Toolbox. We suggested the following: given the importance of the GRB detection in multi-messenger observations, we propose to include an extra drop-down menu in the Toolbox, where one can choose a GRB instrument along with a GW detector. For each simulated GW event (i.e. BNS or BH-NS), the Toolbox would then compute the peak GRB flux detected by the specified EM instrument. This peak flux would be added to the catalogue that is the output of the Toolbox. Additionally, the Toolbox would print the number of joint GRB-GW detections that would be done in the specified setup. Moreover, we intend to allow the user to select a certain photometric filter in which one wants to investigate the KN that results from the merger. The peak magnitude within this filter would also be added to the catalogue, for every GW event. For BBHs, we propose to allow the user to choose one of the different models we have listed. The luminosity estimate will be added as an extra column to the catalogue.

All in all, we now have a very solid set of mathematical frameworks for EM models to GW sources. With the proposed implementation, all that is left is to actually perform this implementation by including these models in the environment of the GW Toolbox. This can be done very soon. If necessary, future improvements that have been suggested throughout this thesis can eventually be added to the EM models. In any case, we will soon have a Toolbox that will start to live up to its full potential. It will be a great benefit for anyone doing GW-related research within the multi-messenger astronomy era.

6 Acknowledgements

I would like to thank my supervisors, Prof. Gijs Nelemans and Dr. Shu-Xu Yi, for their devotion to my project and all their help to create a succesful outcome. Through aiding me with in-depth examination of my models, as well as useful advice that I have been given in numerous meetings, they have guided me through my project exceptionally. Additionally, as a result of the fruitful discussions I have had with them over the past year, this project has been especially enjoyable. I am looking forward to staying in touch with them to possibly have more collaborations and/or discussions in the future. I would also like to express my gratitude to Andrew Toivonen, Prof. Tim Dietrich, and Dr. Michael Coughlin for their efforts in providing me with help and information regarding the KN model. Moreover, I am grateful to all members of the weekly stellar evolution and bi-weekly GW meetings, as these have, despite being online, often been very insightful. Lastly, I would like to mention my partner, housemates, friends and family, whose company and encouragement have made life during a pandemic really not so bad at all.

References

- [1] B. P. Abbott et al. “Binary Black Hole Population Properties Inferred from the First and Second Observing Runs of Advanced LIGO and Advanced Virgo”. In: *The Astrophysical Journal* 882.2 (11th Sept. 2019), p. L24. ISSN: 2041-8213. DOI: 10.3847/2041-8213/ab3800.
- [2] B. P. Abbott et al. “LIGO: the Laser Interferometer Gravitational-Wave Observatory”. In: *Reports on Progress in Physics* 72.7 (1st July 2009), p. 076901. ISSN: 0034-4885, 1361-6633. DOI: 10.1088/0034-4885/72/7/076901.
- [3] B. P. Abbott et al. “Multi-messenger Observations of a Binary Neutron Star Merger”. In: *The Astrophysical Journal* 848.2 (16th Oct. 2017), p. L12. ISSN: 2041-8213. DOI: 10.3847/2041-8213/aa91c9.
- [4] B. Abbott et al. “GW170817: Observation of Gravitational Waves from a Binary Neutron Star Inspiral”. In: *Physical Review Letters* 119.16 (16th Oct. 2017), p. 161101. ISSN: 0031-9007, 1079-7114. DOI: 10.1103/PhysRevLett.119.161101.
- [5] B. Abbott et al. “Observation of Gravitational Waves from a Binary Black Hole Merger”. In: *Physical Review Letters* 116.6 (11th Feb. 2016), p. 061102. ISSN: 0031-9007, 1079-7114. DOI: 10.1103/PhysRevLett.116.061102.
- [6] R. Abbott et al. “GW190521: A Binary Black Hole Merger with a Total Mass of 150 M_{\odot} ”. In: *Physical Review Letters* 125.10 (2nd Sept. 2020), p. 101102. ISSN: 0031-9007, 1079-7114. DOI: 10.1103/PhysRevLett.125.101102.
- [7] F. Acernese et al. “Advanced Virgo: a second-generation interferometric gravitational wave detector”. In: *Classical and Quantum Gravity* 32.2 (22nd Jan. 2015), p. 024001. ISSN: 0264-9381, 1361-6382. DOI: 10.1088/0264-9381/32/2/024001.
- [8] P. Amaro-Seoane et al. “Laser Interferometer Space Antenna”. In: *arXiv:1702.00786 [astro-ph]* (23rd Feb. 2017). arXiv: 1702.00786.
- [9] S. Ascenzi et al. “Electromagnetic Counterparts of Compact Binary Mergers”. In: *Journal of Plasma Physics* 87.1 (Feb. 2021), p. 845870102. ISSN: 0022-3778, 1469-7807. DOI: 10.1017/S0022377820001646. arXiv: 2011.04001.
- [10] D. Band et al. “BATSE observations of gamma-ray burst spectra. I - Spectral diversity”. In: *The Astrophysical Journal* 413 (Aug. 1993), p. 281. ISSN: 0004-637X, 1538-4357. DOI: 10.1086/172995.
- [11] I. Bartos et al. “Rapid and Bright Stellar-mass Binary Black Hole Mergers in Active Galactic Nuclei”. In: *The Astrophysical Journal* 835.2 (27th Jan. 2017), p. 165. ISSN: 1538-4357. DOI: 10.3847/1538-4357/835/2/165.
- [12] S. Bernuzzi. “Neutron star merger remnants”. In: *General Relativity and Gravitation* 52.11 (Nov. 2020), p. 108. ISSN: 0001-7701, 1572-9532. DOI: 10.1007/s10714-020-02752-5.

-
- [13] R. D. Blandford and R. L. Znajek. “Electromagnetic extraction of energy from Kerr black holes”. In: *Monthly Notices of the Royal Astronomical Society* 179.3 (1st July 1977), pp. 433–456. ISSN: 0035-8711, 1365-2966. DOI: 10.1093/mnras/179.3.433.
- [14] T. Bode et al. “Mergers of Supermassive Black Holes in Astrophysical Environments”. In: *The Astrophysical Journal* 744.1 (1st Jan. 2012), p. 45. ISSN: 0004-637X, 1538-4357. DOI: 10.1088/0004-637X/744/1/45. arXiv: 1101.4684.
- [15] M. Bulla. “possis: predicting spectra, light curves, and polarization for multidimensional models of supernovae and kilonovae”. In: *Monthly Notices of the Royal Astronomical Society* 489.4 (11th Nov. 2019), pp. 5037–5045. ISSN: 0035-8711, 1365-2966. DOI: 10.1093/mnras/stz2495.
- [16] M. Campanelli et al. “Large Merger Recoils and Spin Flips from Generic Black Hole Binaries”. In: *The Astrophysical Journal* 659.1 (10th Apr. 2007), pp. L5–L8. ISSN: 0004-637X, 1538-4357. DOI: 10.1086/516712.
- [17] R. Ciolfi. “Short gamma-ray burst central engines”. In: *International Journal of Modern Physics D* 27.13 (Oct. 2018), p. 1842004. ISSN: 0218-2718, 1793-6594. DOI: 10.1142/S021827181842004X. arXiv: 1804.03684.
- [18] P. Collaboration et al. “Planck 2018 results. I. Overview and the cosmological legacy of Planck”. In: *Astronomy & Astrophysics* 641 (Sept. 2020), A1. ISSN: 0004-6361, 1432-0746. DOI: 10.1051/0004-6361/201833880. arXiv: 1807.06205.
- [19] M. W. Coughlin et al. “Constraints on the neutron star equation of state from AT2017gfo using radiative transfer simulations”. In: *Monthly Notices of the Royal Astronomical Society* 480.3 (1st Nov. 2018), pp. 3871–3878. ISSN: 0035-8711, 1365-2966. DOI: 10.1093/mnras/sty2174.
- [20] M. W. Coughlin et al. “Measuring the Hubble constant with a sample of kilonovae”. In: *Nature Communications* 11.1 (Dec. 2020), p. 4129. ISSN: 2041-1723. DOI: 10.1038/s41467-020-17998-5.
- [21] S. d’Ascoli et al. “Electromagnetic Emission from Supermassive Binary Black Holes Approaching Merger”. In: *The Astrophysical Journal* 865.2 (2nd Oct. 2018), p. 140. ISSN: 1538-4357. DOI: 10.3847/1538-4357/aad8b4.
- [22] R. Fernández and B. D. Metzger. “Electromagnetic Signatures of Neutron Star Mergers in the Advanced LIGO Era”. In: *Annual Review of Nuclear and Particle Science* 66.1 (19th Oct. 2016), pp. 23–45. ISSN: 0163-8998, 1545-4134. DOI: 10.1146/annurev-nucl-102115-044819.
- [23] W. Fong et al. “A DECADE OF SHORT-DURATION GAMMA-RAY BURST BROADBAND AFTERGLOWS: ENERGETICS, CIRCUMBURST DENSITIES, AND JET OPENING ANGLES”. In: *The Astrophysical Journal* 815.2 (15th Dec. 2015), p. 102. ISSN: 1538-4357. DOI: 10.1088/0004-637X/815/2/102.

-
- [24] D. A. Frail et al. “Beaming in Gamma-Ray Bursts: Evidence for a Standard Energy Reservoir”. In: *The Astrophysical Journal* 562.1 (20th Nov. 2001), pp. L55–L58. ISSN: 0004637X. DOI: 10.1086/338119.
- [25] C. L. Fryer et al. “THE FATE OF THE COMPACT REMNANT IN NEUTRON STAR MERGERS”. In: *The Astrophysical Journal* 812.1 (5th Oct. 2015), p. 24. ISSN: 1538-4357. DOI: 10.1088/0004-637X/812/1/24.
- [26] A. Goldstein et al. “An Ordinary Short Gamma-Ray Burst with Extraordinary Implications: *Fermi* -GBM Detection of GRB 170817A”. In: *The Astrophysical Journal* 848.2 (16th Oct. 2017), p. L14. ISSN: 2041-8213. DOI: 10.3847/2041-8213/aa8f41.
- [27] J. A. González et al. “Supermassive Recoil Velocities for Binary Black-Hole Mergers with Antialigned Spins”. In: *Physical Review Letters* 98.23 (7th June 2007), p. 231101. ISSN: 0031-9007, 1079-7114. DOI: 10.1103/PhysRevLett.98.231101.
- [28] M. Graham et al. “Candidate Electromagnetic Counterpart to the Binary Black Hole Merger Gravitational-Wave Event S190521g”. In: *Physical Review Letters* 124.25 (25th June 2020), p. 251102. ISSN: 0031-9007, 1079-7114. DOI: 10.1103/PhysRevLett.124.251102.
- [29] M. Gröbner et al. “Binary black hole mergers in AGN accretion discs: gravitational wave rate density estimates”. In: *Astronomy & Astrophysics* 638 (June 2020), A119. ISSN: 0004-6361, 1432-0746. DOI: 10.1051/0004-6361/202037681.
- [30] G. M. Harry and the LIGO Scientific Collaboration. “Advanced LIGO: the next generation of gravitational wave detectors”. In: *Classical and Quantum Gravity* 27.8 (21st Apr. 2010), p. 084006. ISSN: 0264-9381, 1361-6382. DOI: 10.1088/0264-9381/27/8/084006.
- [31] J. B. Hartle. *Gravity: an introduction to Einstein’s general relativity*. San Francisco: Addison-Wesley, 2003. 582 pp. ISBN: 978-0-8053-8662-2.
- [32] G. Hobbs and S. Dai. “Gravitational wave research using pulsar timing arrays”. In: *National Science Review* 4.5 (1st Sept. 2017), pp. 707–717. ISSN: 2095-5138, 2053-714X. DOI: 10.1093/nsr/nwx126.
- [33] K. Ioka and T. Nakamura. “Can an Off-axis Gamma-Ray Burst Jet in GW170817 Explain All the Electromagnetic Counterparts?” In: *arXiv:1710.05905 [astro-ph, physics:gr-qc]* (8th Apr. 2018). arXiv: 1710.05905.
- [34] K. Ioka and T. Nakamura. “Peak Luminosity–Spectral Lag Relation Caused by the Viewing Angle of the Collimated Gamma-Ray Bursts”. In: *The Astrophysical Journal* 554.2 (20th June 2001), pp. L163–L167. ISSN: 0004637X. DOI: 10.1086/321717.
- [35] K. Ioka and T. Nakamura. “Spectral puzzle of the off-axis gamma-ray burst in GW170817”. In: *Monthly Notices of the Royal Astronomical Society* 487.4 (21st Aug. 2019), pp. 4884–4889. ISSN: 0035-8711, 1365-2966. DOI: 10.1093/mnras/stz1650.

-
- [36] D. Kasen et al. “Origin of the heavy elements in binary neutron-star mergers from a gravitational-wave event”. In: *Nature* 551.7678 (2nd Nov. 2017), pp. 80–84. ISSN: 0028-0836, 1476-4687. DOI: 10.1038/nature24453.
- [37] B. J. Kelly et al. “Electromagnetic Emission from a Binary Black Hole Merger Remnant in Plasma: Field Alignment and Plasma Temperature”. In: *Physical Review D* 103.6 (26th Mar. 2021), p. 063039. ISSN: 2470-0010, 2470-0029. DOI: 10.1103/PhysRevD.103.063039. arXiv: 2010.11259.
- [38] B. J. Kelly et al. “Prompt electromagnetic transients from binary black hole mergers”. In: *Physical Review D* 96.12 (12th Dec. 2017), p. 123003. ISSN: 2470-0010, 2470-0029. DOI: 10.1103/PhysRevD.96.123003.
- [39] A. Khan et al. “Disks Around Merging Binary Black Holes: From GW150914 to Supermassive Black Holes”. In: *Physical Review D* 97.4 (23rd Feb. 2018), p. 044036. ISSN: 2470-0010, 2470-0029. DOI: 10.1103/PhysRevD.97.044036. arXiv: 1801.02624.
- [40] J. H. Krolik. “Estimating the Prompt Electromagnetic Luminosity of a Black Hole Merger”. In: *The Astrophysical Journal* 709.2 (1st Feb. 2010), pp. 774–779. ISSN: 0004-637X, 1538-4357. DOI: 10.1088/0004-637X/709/2/774.
- [41] G. P. Lamb and S. Kobayashi. “GRB 170817A as a jet counterpart to gravitational wave trigger GW 170817”. In: *Monthly Notices of the Royal Astronomical Society* 478.1 (21st July 2018), pp. 733–740. ISSN: 0035-8711, 1365-2966. DOI: 10.1093/mnras/sty1108. arXiv: 1710.05857.
- [42] R. N. Lang and S. A. Hughes. “Advanced localization of massive black hole coalescences with LISA”. In: *Classical and Quantum Gravity* 26.9 (7th May 2009), p. 094035. ISSN: 0264-9381, 1361-6382. DOI: 10.1088/0264-9381/26/9/094035.
- [43] M. Maggiore et al. “Science Case for the Einstein Telescope”. In: *Journal of Cosmology and Astroparticle Physics* 2020.3 (24th Mar. 2020), pp. 050–050. ISSN: 1475-7516. DOI: 10.1088/1475-7516/2020/03/050. arXiv: 1912.02622.
- [44] B. McKernan et al. “Ram-pressure stripping of a kicked Hill sphere: Prompt electromagnetic emission from the merger of stellar mass black holes in an AGN accretion disk”. In: *The Astrophysical Journal* 884.2 (17th Oct. 2019), p. L50. ISSN: 2041-8213. DOI: 10.3847/2041-8213/ab4886. arXiv: 1907.03746.
- [45] B. D. Metzger and E. Berger. “WHAT IS THE MOST PROMISING ELECTROMAGNETIC COUNTERPART OF A NEUTRON STAR BINARY MERGER?” In: *The Astrophysical Journal* 746.1 (10th Feb. 2012), p. 48. ISSN: 0004-637X, 1538-4357. DOI: 10.1088/0004-637X/746/1/48.
- [46] B. D. Metzger. “Kilonovae”. In: *Living Reviews in Relativity* 20.1 (Dec. 2017), p. 3. ISSN: 2367-3613, 1433-8351. DOI: 10.1007/s41114-017-0006-z.

-
- [47] H. Mo, F. Van den Bosch and S White. *Galaxy formation and evolution*. OCLC: 646069565. Cambridge; New York: Cambridge University Press, 2010. ISBN: 978-0-511-72962-1 978-0-511-72632-3 978-0-511-72772-6 978-0-521-85793-2 978-0-511-80724-4.
- [48] V. Nedora et al. "Mapping dynamical ejecta and disk masses from numerical relativity simulations of neutron star mergers". In: *arXiv:2011.11110 [astro-ph, physics:gr-qc]* (22nd Nov. 2020). arXiv: 2011.11110.
- [49] G. Nelemans, L. R. Yungelson and S. F. Portegies Zwart. "The gravitational wave signal from the Galactic disk population of binaries containing two compact objects". In: *Astronomy & Astrophysics* 375.3 (Sept. 2001), pp. 890–898. ISSN: 0004-6361, 1432-0746. DOI: 10.1051/0004-6361:20010683.
- [50] S. Nissanke et al. "Exploring short gamma-ray bursts as gravitational-wave standard sirens". In: *The Astrophysical Journal* 725.1 (10th Dec. 2010), pp. 496–514. ISSN: 0004-637X, 1538-4357. DOI: 10.1088/0004-637X/725/1/496. arXiv: 0904.1017.
- [51] C. D. Ott. "Probing the core-collapse supernova mechanism with gravitational waves". In: *Classical and Quantum Gravity* 26.20 (21st Oct. 2009), p. 204015. ISSN: 0264-9381, 1361-6382. DOI: 10.1088/0264-9381/26/20/204015.
- [52] B. E. J. Pagel. *Nucleosynthesis and chemical evolution of galaxies*. 2nd ed. OCLC: ocn258082983. Cambridge ; New York: Cambridge University Press, 2009. 466 pp. ISBN: 978-0-521-84030-9.
- [53] T. Piran. "Gamma-ray bursts and the fireball model". In: *Physics Reports* 314.6 (June 1999), pp. 575–667. ISSN: 03701573. DOI: 10.1016/S0370-1573(98)00127-6.
- [54] M. J. Rees and P. Meszaros. "Unsteady outflow models for cosmological gamma-ray bursts". In: *The Astrophysical Journal* 430 (Aug. 1994), p. L93. ISSN: 0004-637X, 1538-4357. DOI: 10.1086/187446.
- [55] M. Ruderman. "THEORIES OF GAMMA-RAY BURSTS". In: *Annals of the New York Academy of Sciences* 262.1 (Oct. 1975), pp. 164–180. ISSN: 0077-8923, 1749-6632. DOI: 10.1111/j.1749-6632.1975.tb31430.x.
- [56] N. Sarin and P. D. Lasky. "The evolution of binary neutron star post-merger remnants: a review". In: *arXiv:2012.08172 [astro-ph, physics:gr-qc]* (15th Dec. 2020). arXiv: 2012.08172.
- [57] W. K. Schmidt. "Distance limit for a class of model -ray burst sources". In: *Nature* 271.5645 (Feb. 1978), pp. 525–527. ISSN: 0028-0836, 1476-4687. DOI: 10.1038/271525a0.
- [58] J. D. Schnittman and J. H. Krolik. "The Infrared Afterglow of Supermassive Black Hole Mergers". In: *The Astrophysical Journal* 684.2 (10th Sept. 2008), pp. 835–844. ISSN: 0004-637X, 1538-4357. DOI: 10.1086/590363.

-
- [59] B. F. Schutz. “Networks of gravitational wave detectors and three figures of merit”. In: *Classical and Quantum Gravity* 28.12 (21st June 2011), p. 125023. ISSN: 0264-9381, 1361-6382. DOI: 10.1088/0264-9381/28/12/125023.
- [60] S. J. Smartt et al. “A kilonova as the electromagnetic counterpart to a gravitational-wave source”. In: *Nature* 551.7678 (1st Nov. 2017), pp. 75–79. ISSN: 1476-4687. DOI: 10.1038/nature24303.
- [61] C. Stachie et al. “Perfect is the enemy of good enough: predicting electromagnetic counterparts using low-latency, gravitational-wave data products”. In: *arXiv:2103.01733 [astro-ph, physics:gr-qc]* (2nd Mar. 2021). arXiv: 2103.01733.
- [62] S. A. Usman, J. C. Mills and S. Fairhurst. “Constraining the Inclination of Binary Mergers from Gravitational-wave Observations”. In: *The Astrophysical Journal* 877.2 (28th May 2019), p. 82. ISSN: 1538-4357. DOI: 10.3847/1538-4357/ab0b3e. arXiv: 1809.10727.
- [63] J. P. W. Verbiest et al. “The International Pulsar Timing Array: First Data Release”. In: *Monthly Notices of the Royal Astronomical Society* 458.2 (11th May 2016), pp. 1267–1288. ISSN: 0035-8711, 1365-2966. DOI: 10.1093/mnras/stw347. arXiv: 1602.03640.
- [64] P. Veres et al. “Gamma-ray burst models in light of the GRB 170817A - GW170817 connection”. In: *arXiv:1802.07328 [astro-ph]* (20th Feb. 2018). arXiv: 1802.07328.
- [65] E. Woods and A. Loeb. “Constraints on Off-Axis X-Ray Emission from Beamed Gamma-Ray Bursts”. In: *The Astrophysical Journal* 523.1 (20th Sept. 1999), pp. 187–191. ISSN: 0004-637X, 1538-4357. DOI: 10.1086/307738.
- [66] S.-X. Yi and K. S. Cheng. “Where Are the Electromagnetic-wave Counterparts of Stellar-mass Binary Black Hole Mergers?” In: *The Astrophysical Journal* 884.1 (7th Oct. 2019), p. L12. ISSN: 2041-8213. DOI: 10.3847/2041-8213/ab459a.
- [67] S.-X. Yi et al. “The Gravitational Wave Universe Toolbox: A software package to simulate observation of the Gravitational Wave Universe with different detectors”. In: *arXiv:2106.13662 [astro-ph]* (25th June 2021). arXiv: 2106.13662.
- [68] C. Yuan et al. “Post-Merger Jets from Supermassive Black Hole Coalescences as Electromagnetic Counterparts of Gravitational Wave Emission”. In: *The Astrophysical Journal Letters* 911.1 (1st Apr. 2021), p. L15. ISSN: 2041-8205, 2041-8213. DOI: 10.3847/2041-8213/abee24. arXiv: 2101.05788.